

P-43

---

# Preliminary Flight-Determined Subsonic Lift and Drag Characteristics of the X-29A Forward-Swept-Wing Airplane

---

John W. Hicks and Thomas Huckabone

---

(NASA-TM-100409) PRELIMINARY  
FLIGHT-DETERMINED SUBSONIC LIFT AND DRAG  
CHARACTERISTICS OF THE X-29A  
FORWARD-SWEPT-WING AIRPLANE (NASA) 43 p

N91-29177

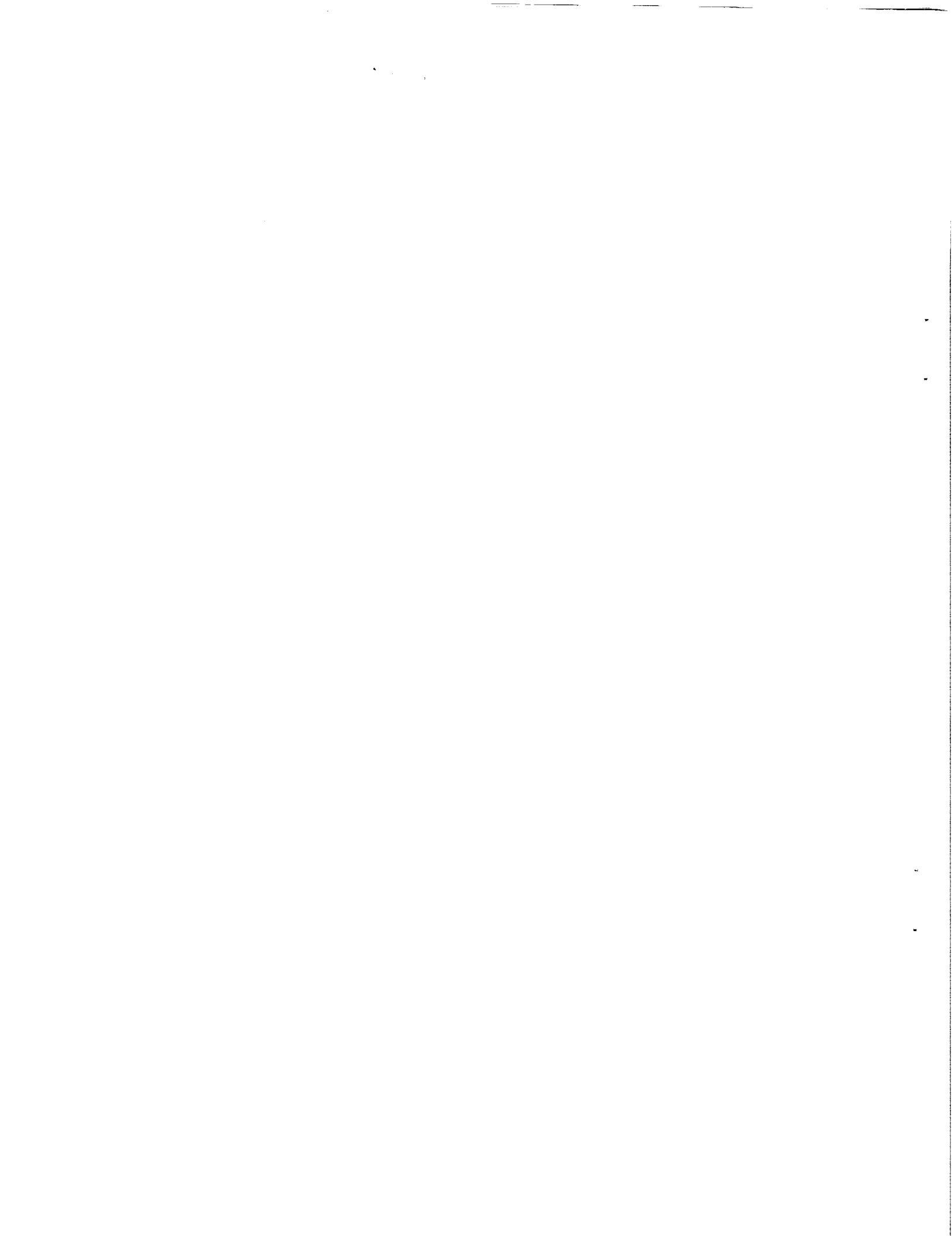
CSCL 01C 63/05

Unclass  
0038501

August 1989

**NASA**  
National Aeronautics and  
Space Administration

Date for general release August 1991



---

# **Preliminary Flight-Determined Subsonic Lift and Drag Characteristics of the X-29A Forward-Swept-Wing Airplane**

---

John W. Hicks and Thomas Huckabone  
Ames Research Center, Dryden Flight Research Facility, Edwards, California

1989



National Aeronautics and  
Space Administration

**Ames Research Center**

Dryden Flight Research Facility  
Edwards, California 93523-5000



# CONTENTS

SUMMARY	1
INTRODUCTION	1
NOMENCLATURE	1
SYSTEM DESCRIPTION	3
Forward-Swept-Wing Concept Benefits	3
Other Technology Concepts	4
X-29A Aircraft	4
General Description	4
Wing	5
Canard, Strake, and Rudder	5
Flight Control System	5
Propulsion System	5
F404 Engine	5
Inlets	5
Aircraft Mass Properties	5
Instrumentation Description	5
WIND TUNNEL MODEL AND DATABASE	6
FLIGHT TEST MANEUVERS	7
DATA ANALYSIS	7
Accelerometer Data Reduction Technique	7
In-Flight Thrust Calculation Procedure	7
Noseboom Angle-of-Attack Calibration	8
Drag Correction Procedure	9
Aerodynamic Drag Corrections	9
Propulsion Drag Corrections	9
Drag Polar Shape Comparison Methods	10
Trimmed and Untrimmed Prediction Comparisons	10
Comparison Methods With Other Aircraft	10
RESULTS AND DISCUSSION	10
Aircraft Configuration Changes	10
Drag Polar Results	11
FUTURE WORK	13
CONCLUSIONS	13
REFERENCES	14
APPENDIX — DATA REDUCTION	15
TABLES	18
FIGURES	22



## SUMMARY

The X-29A subsonic lift and drag characteristics determined, met, or exceeded predictions, particularly with respect to the drag polar shapes. Induced drag levels were as great as 20 percent less than wind tunnel estimates, particularly at coefficients of lift above 0.8. Drag polar shape comparisons with other modern fighter aircraft showed the X-29A to have a better overall aircraft aerodynamic Oswald efficiency factor for the same aspect ratio. Two significant problems arose in the data reduction and analysis process. These included uncertainties in angle-of-attack upwash calibration and effects of maneuver dynamics on drag levels. The latter problem resulted from significantly improper control surface automatic camber control scheduling. Supersonic drag polar results were not obtained during this phase because of a lack of engine instrumentation to measure afterburner fuel flow.

## INTRODUCTION

Fighter aircraft need efficient transonic aerodynamics. To achieve this, wing sweep was introduced to increase the drag-rise Mach number and decrease drag in the early 1950s. Aft sweep was used at that time because of the structural divergence problem of forward-swept wings. Recently, with the advent of high-strength materials and aeroelastic tailoring, it has become feasible to incorporate forward-wing sweep without prohibitive weight penalties (Krone, 1975). Studies spanning over 50 years indicated that for a given transonic maneuver capability, a forward-swept wing would outperform an aft-swept wing.

To investigate the potential performance benefits and to assess the problems associated with forward-swept wings, NASA and the Department of Defense have been conducting a forward-swept-wing technology demonstrator program. This demonstrator aircraft, termed the X-29A, has been flown at the NASA Ames Research Center's Dryden Flight Research Facility (Sefic and Cutler, 1986). Hicks and Matheny (1987) presented preliminary flight results from the flight envelope expansion phase.

One of the major objectives of the X-29A program was to determine the aerodynamic performance of the forward-swept wing. Dynamic pushover-pullup and windup turn maneuvers determined aerodynamic characteristics and calculated inflight thrust. These data have been used to calculate drag polar data over the subsonic flight envelope. Emphasis was on aeroperformance derived from standard accelerometer test techniques rather than classical point performance. Primary interest was in obtaining induced drag polar shapes, with less emphasis on measuring absolute drag levels. Engine instrumentation limitations prevented obtaining supersonic drag data. Flight envelope boundaries during this phase included a maximum supersonic Mach number of 1.50, altitude of 50,000 ft, angle of attack of 20°, and normal load factor of 5.7 *g*. This paper presents preliminary drag polar data obtained during the flight envelope expansion phase and compares the data to the predictions. Also presented is a description of the X-29A, including the configuration geometry, propulsion system, control system, instrumentation, and techniques used to derive the drag polar results.

In addition to the forward-swept wing, the X-29A incorporated several advanced technologies for evaluation. These included a close-coupled wing/canard configuration, thin supercritical airfoil for the wing, aeroelastically tailored composite wing skins, three-surface pitch control, and active flight controls.

## NOMENCLATURE

A	geometric area, in. <sup>2</sup>
ACAP	inlet capture area
ACC	wing flaperon automatic camber control
AREF	nozzle reference area
ASW	aft-swept wing

$c$	wing chord length, in.
$C_{FG}$	gross thrust coefficient
c.g.	aircraft center of gravity
$C_D$	coefficient of drag
$C_{Di}$	coefficient of induced drag
$C_{Dmin}$	coefficient of parasite drag
$C_L$	coefficient of lift
CS	canard station
DINT	nozzle interference drag
DSPILL	inlet spillage drag
FDMS	flight deflection measurement system
$FG$	gross thrust, lb
$FGI$	ideal gross thrust, lb
FM	frequency modulation
$FN$	net thrust, lb
$FR$	ram drag, lb
FRL	fuselage reference line
FS	fuselage station
FSW	forward-swept wing
FVG	fan guide vanes
$g$	earth acceleration
$H$	enthalpy, Btu
HiMAT	highly maneuverable aircraft technology
HPC	high-pressure compressor
HPVG	high-pressure compressor guide vanes
$L/D$	lift-to-drag ratio
LED	light-emitting diode
LPT	low-pressure turbine
$M$	Mach number
MAC	mean aerodynamic chord
MCC	wing flaperon manual camber control
N1	low-pressure compressor rotor speed, rpm
N2	high-pressure compressor rotor speed, rpm
$n_{xw}$	aircraft wind-axis longitudinal acceleration, $g$
$n_{zw}$	aircraft wind-axis normal acceleration, $g$
PCM	pulse-code modulation
PLA	power lever angle, deg
PLF	power for level flight
PS	static pressure, lb/in. <sup>2</sup>
PT	total pressure, lb/in. <sup>2</sup>
$\bar{q}$	dynamic pressure, lb/ft <sup>2</sup>
TT	total temperature, °F
UFTAS	uniform flight test analysis system
$V$	velocity, ft/sec
$W$	mass flow, lb/sec
WFAB	afterburner fuel flow, lb/sec
WFE	main engine fuel flow, lb/sec
WFP	afterburner pilot fuel flow, lb/sec

WFT	total fuel flow, lb/sec
WL	water line station
WS	wing station
$\alpha$	angle of attack
$\beta$	angle of sideslip
$\delta_c$	canard deflection angle, deg
$\delta_f$	flaperon deflection angle, deg
$\delta_s$	strake flap deflection angle, deg
$\theta_{TWIST}$	airfoil twist angle

#### Engine station numbers:

0	free stream
1	compressor face
25	high-pressure compressor inlet
3	high-pressure compressor discharge
4	combustor discharge
5	low-pressure turbine rotor discharge (after LPT cooling air mix)
558	low-pressure turbine discharge (measuring plane)
6	afterburner inlet
7	exhaust nozzle inlet
8	exhaust nozzle throat
9	exhaust nozzle discharge

## SYSTEM DESCRIPTION

### Forward-Swept-Wing Concept Benefits

The forward-swept-wing (FSW) concept promises significant performance advantages in the transonic speed regime that may lead to new airframe design freedoms and options. These include such things as a reduction in aircraft size and gross weight, dependent on mission, while simultaneously increasing volumetric efficiency around the aircraft center of gravity. The FSW has been predicted to save up to 13 percent in aircraft drag for wings of the same aspect ratio because of a substantial reduction in transonic wing profile drag compared with an aft-swept wing (ASW) of the same aspect ratio, taper ratio, wing area, and shock location and sweep. This is primarily because the FSW requires less leading edge sweep for the same shock sweep and location, which results in less wing twist required to control spanwise flow and a reduction in the pressure drag contribution of the shock. The corresponding greater sweep of the FSW trailing edge results in a greater shock sweep angle that reduces the shock strength, in turn, reducing the wave drag and the drag due to shock-induced flow separation. The geometrical differences between the FSW and ASW with the same shock sweep angle yield a shorter wing box length for the FSW of the same aspect ratio and taper ratio. This lowers the wing box bending load and structural weight or, conversely, allows an increase in the aspect ratio for the same bending load. The allowable increase in aspect ratio has an additional advantage of increasing aerodynamic efficiency and reducing the induced drag of the wing by as much as a predicted additional 8 percent. The FSW is predicted to exhibit better lateral control at higher angles of attack than an ASW design because of the inboard flow of air over the top of the wing, which inhibits wingtip stall and, thus, loss of aileron effectiveness as angle of attack increases.

## Other Technology Concepts

The technology of using advanced composites, coupled with aeroelastic tailoring of those composites in the wing skins, allowed the FSW to have enough structural integrity to resist its natural tendency toward structural divergence. Another objective was to demonstrate advanced flight control techniques in stabilizing and controlling an unstable airframe with a close-coupled wing/canard and a three-surface pitch control system. The unusually large, relaxed longitudinal static stability has the potential advantage of increasing transonic and high angle-of-attack maneuverability while reducing trim drag changes with changing flight condition and enhancing overall aerodynamic efficiency. The close-coupled wing/canard configuration allows for a better combined elliptical lift distribution than with the wing alone. The canard also improves aircraft maneuverability and performance by contributing a positive lift component to the wing lift for trimming, in contrast to an aft-mounted horizontal tail that produces a download for trim, reducing net aircraft lift. The canard inhibits the FSW natural tendency toward wing root stall by injecting high-energy air into the root region and by reducing the wing local angle of attack with canard downwash.

Other advanced technologies to improve aircraft performance include the supercritical wing airfoil and the wing flaperon automatic camber control (ACC) mode. The value of the supercritical airfoil was to improve transonic performance by delaying transonic wave drag rise to a higher subsonic Mach number. The ACC feature achieves better off-design performance while maneuvering.

## X-29A Aircraft

**General Description.** The X-29A advanced technology demonstrator (fig. 1) is a single-seat, fighter-type aircraft incorporating several new technology concepts that synergistically improve aircraft performance. A special feature of the aircraft was its active three-surface pitch control configuration. In addition to the wing flaperons, this included the forward-mounted canards and the aft-mounted strake flaps. Extensive use was made of available hardware not directly related to the advanced technologies, including the F-5A forward fuselage and nose gear forward of the X-29A inlets, F-16 main landing gear and servo-actuators, and F-14 avionics.

**Wing.** The most notable feature is the forward-swept wing with a  $29.3^\circ$  leading edge sweep, an aspect ratio of 4.0, and a thin supercritical airfoil section with a thickness-to-chord ratio of 5 percent. The FSW has a Grumman K, Mod 2 supercritical airfoil cross section with a mean aerodynamic chord of 86.6 in. and a built-in wing leading edge root-to-tip twist designed to optimize transonic performance at Mach 0.90. This airfoil was originally developed by the manufacturer for the HiMAT vehicle research competition. The wing twist distribution along the semispan is shown in figure 2. The airfoil has a design coefficient of lift of 0.92 at the transonic Mach 0.90 condition. The upper and lower surface wing skins are of a graphite-epoxy composite to aeroelastically tailor the wing deflection and inhibit wing structural divergence. The composite layup of up to 156 plies consists of  $0^\circ/90^\circ/+45^\circ$  laminated strips of AS/3501/5A graphite-epoxy tape with the primary plies outboard of wing station 64, oriented  $9^\circ$  forward of the wing structural line axis. The wing has no leading edge devices but incorporates full-span trailing edge, dual-hinged flaperons divided into three segments on the wing. The midwing and outboard segments are driven by a single hydraulic actuator, housed in a fairing under the wing (fig. 3). The oversized fairing was necessary because of the use of large government-furnished F-16 actuators. The inboard segment is driven by a separate actuator located near the wing root. The flaperons automatically vary the camber of the wing for high lift during takeoff and landing and increase aerodynamic efficiency over the flight envelope. Full flaperon travel was from  $10^\circ$  trailing edge up to  $24.75^\circ$  trailing edge down. The maximum flaperon deflection rate is  $68^\circ/\text{sec}$ . The wing root forward surface extensions of the wing were added as an aerodynamic fairing and have no structural function. The aerodynamic reference area of  $185 \text{ ft}^2$  does not include the canards or strake flaps and only includes the geometric projection of the trapezoidal wing surface into the aircraft body without the forward surface extensions at the wing root leading edge.

**Canard, Strake, and Rudder.** The canards constitute 20 percent of the wing area and act as a powerful lift and pitch generator. They are of a single-piece construction and travel 30° leading edge up to 60° leading edge down, moving at rates of up to 100°/sec. The canards are symmetric airfoils with zero twist (fig. 2). The wing is integrated into the fuselage using bodymounted strakes that extend to the aft end of the fuselage. The single-piece strake flaps at the end of the body strakes travel from 30° trailing edge up to 30° trailing edge down. A single-piece rudder completes the aerodynamic control configuration. Table 1 summarizes the aerodynamic surface geometries.

**Flight Control System.** The presence of the canards results in an otherwise neutrally stable airframe having a negative static margin of nominally 35 percent. The large negative static margin reduced trim drag and produced better maneuverability. This high degree of instability necessitates high levels of artificial stability augmentation provided by the triplex digital fly-by-wire flight control system. The flight control system updates the stabilization of the aircraft state at 40 Hz and consists of three primary flight modes: the prime normal digital mode, the digital reversion mode, and the analog reversion mode. Each mode has both a "clean" or cruise aircraft gain scheduling, known as "up and away," and a power approach gain scheduling. The flight control system provided trim and pitch control integrally for symmetric deflection of three-surface pitch control configuration. Differential deflection of the flaperons provided the sole source of roll control. The single-piece rudder provided yaw control. The control system featured aileron-to-rudder interconnect. The two wing camber control modes included the ACC, set by the flight control system as a function of flight condition, and the manual camber control (MCC), set in discrete 5° intervals by the pilot. The MCC mode was primarily a flight test mode. Figure 4 depicts the range and function of the flaperon settings.

### **Propulsion System.**

*F404 Engine.* The X-29A is powered by a General Electric F404-GE-400 turbofan engine, rated at 16,000 lb thrust at sea level static conditions. This low-bypass fan engine with afterburner consists of a three-stage fan driven by a single-stage, low-pressure turbine and a seven-stage, high-pressure compressor driven by a single-stage, high-pressure turbine.

*Inlets.* Two fuselage-mounted side inlets supply air to the engine (fig. 5) by a bifurcated duct, ending 18 in. in front of the compressor face. To give optimum transonic performance, the inlets are of a simple, fixed-geometry design with a 15° swept splitter plate and elliptical-inlet cowl lip geometry for good static inlet performance and compatibility.

**Aircraft Mass Properties.** Maximum aircraft takeoff gross weight is 17,800 lb with a 4000-lb JP-5 fuel capacity in two fuselage and two strake tanks. Total fuel capacity was divided into 1700 lb in the forward fuel tank, 1700 lb in the feed tank, and 300 lb located in each strake tank. The aircraft had no in-flight refueling capability. The wings were dry with no integral fuel tanks. Center of gravity range with landing gear up was small, with maximum fuselage station variation from approximately 438 in. to 449 in. or from -25.7 percent MAC to -13.0 percent MAC, respectively.

### **Instrumentation Description**

The data parameter set included measurements for structural loads, structural dynamics, flight controls, stability and control, aircraft subsystems, propulsion, and performance. Instrumentation included accelerometers, rate gyros, strain gages, aerodynamic pressure taps, temperature and pressure monitors, a noseboom pitot-static system with

angle-of-attack and angle-of-sideslip angle vanes, control surface position and rate monitors, and a basic thrust instrumentation set for the engine. The thrust instrumentation consisted of pressure, temperature, compressor speeds, nozzle area, and main engine fuel flow measurements for engine operation monitoring as well as a limited ability to calculate in-flight thrust levels. An engine schematic showing engine station, engine components, and measured parameters is shown in figure 6. The aircraft contained two body-mounted, three-axis accelerometer packages for performance and other measurements.

The X-29A instrumentation system (fig. 7) measured a total of 691 data parameters telemetered to the ground for recording, real-time analysis, and control room monitoring. The aircraft did not have an onboard recording capability. The 10-bit remote unit pulse-code modulation (PCM) system sampled data from 25 to 400 samples/sec, depending on the desired frequency range to be covered. The digital data were processed by five PCM units that merged the data stream along with the output from the flight control computers *ARINC 429 (Aeronautical Radio, Inc.)* data bus using an interleaver device. Onboard filtering was restricted to antialiasing filters only. The encrypted data were downlinked as a single serial PCM stream. A constant-bandwidth frequency modulation (FM) system was installed to process high-response acceleration and vibration data. This FM signal was merged with the rest of the digital data from the interleaver and downlinked along with the pilot's voice. All telemetered data were received by a ground station and relayed to the mission control center for real-time processing and display.

External aircraft instrumentation included the pitot-static noseboom with angle-of-attack and angle-of-sideslip angle vanes (fig. 8). The left side of the aircraft had 176 flush-mounted static pressure orifices, located in two rows on the canard, five rows on the wing, and one row along the strake and strake flap to measure pressure distribution (fig. 9). The right wing contained 12 infrared light-emitting diodes (LEDs) mounted on the top of the wing as part of the flight deflection measurement system (FDMS). These LED targets ranged in size from 0.25 to 1.50 in. in height. A dual receiver was mounted in the right side of the fuselage above the wing root (fig. 10). Finally, the underside of each wing contained an aerodynamic fairing that contained a flight test eccentric rotary-mass flaperon structural excitation system, in addition to housing the midboard and outboard flaperon hydraulic-actuator.

Once received on the ground, the data were decommutated and recorded in real time on magnetic tapes for postflight data processing. Data were also processed in real time by conversion to engineering units, filtered and sampled where necessary, and displayed in the control room during the missions. Real-time computations were made with some of the flight data through real-time minicomputers and displayed in real time against predictions that were generated either preflight or in real time using actual flight states provided from the downlinked aircraft data. Data were displayed on analog time-history strip charts as digital data or plotted graphically on video screens and through various analog gauges and display lights in the control room.

## WIND TUNNEL MODEL AND DATABASE

Several different wind tunnel and developmental FSW models were tested to determine the final X-29A configuration. The final configuration was tested mostly at the NASA Ames Research Center's 11-ft and 9- by 7-ft wind tunnels, running at Reynolds numbers from 1 to  $2 \times 10^6$ . The primary wind tunnel model was a rigid 1/8-scale model, configured for the Mach 0.90, 30,000 ft design condition. Some 1368 wind tunnel hours were used to develop the X-29A configuration. Facilities, tests, and run times are shown in table 2. Runs were made over a range of angle of attack up to  $24^\circ$  and sideslip angles to  $12^\circ$  at discrete Mach numbers up to 1.4. Control surfaces were set in 5 to  $10^\circ$  discrete increments over their full travel range and separate measurements made at each configuration setting. The main objectives of the wind tunnel tests were not to develop accurate drag polar models, but rather to gather structural load information and to develop an aerodynamics database for the development of the flight control system. Airframe drag component buildup measurements were made, but sensitive wind tunnel drag balances were not used to measure full configuration drag levels. Inlet and nozzle model drag measurements were not made. The wind tunnel-generated aerodynamic database was corrected for flexible structural effects using analytical predictions. Details of the wind tunnel tests can be found in Charletta (1982) and Bowers (1984).

## FLIGHT TEST MANEUVERS

Drag polar data was obtained using pushover-pullup and windup turn dynamic flight test technique maneuvers and 1-g stabilized points. The pushover-pullup was initiated from a stabilized 1-g flight condition at power for level flight (PLF). The aircraft then began a pushover to zero  $g$  normal load factor at 0.2  $g$ /sec  $g$ -onset rate. A pullup was then made to 2  $g$ , and a recovery to the 1-g flight condition completed the 20-sec maneuver. The constant Mach windup turn maneuvers consisted of two different techniques. One was a constant PLF maneuver where altitude is traded to hold constant Mach as normal load factor increased to the aim load factor or limit alpha (15° maximum). The second method held constant altitude by increasing engine power to keep constant Mach as load factor was increased to its aim value or limit alpha. The 1-g stabilized points determined position error and angle-of-attack calibration data. Details of the X-29A flight test maneuver techniques are in Hicks and others (1987).

## DATA ANALYSIS

### Accelerometer Data Reduction Technique

The computer analysis program used was the uniform flight test analysis system (UFTAS) developed by the Air Force Flight Test Center. This program consists of several subroutines that can compute flightpath accelerations by several methods, including several accelerometer techniques. It also applies data corrections and computes test day point-performance or drag polars. The UFTAS contains an in-flight thrust subroutine that not only allows propulsion and test-day performance calculations, but with other subroutines in the program calculates standard-day thrust and performance. Further details of the computer program appear in Air Force Flight Test Center, Edwards AFB (1973).

Aerodynamic drag polar data reduction was accomplished using the accelerometer method to determine longitudinal and vertical (normal) accelerations in the aircraft flightpath axis system. The results were used to compute coefficient of lift ( $C_L$ ) from the vertical or normal acceleration and coefficient of drag ( $C_D$ ) by using the longitudinal acceleration to compute excess thrust. This was subtracted from thrust available to obtain thrust required and, thus, drag. A body-mounted accelerometer system was used, which consisted of two separate instrumentation packages. The first, called the center of gravity (c.g.) or coarse accelerometer package, covered a broader acceleration range of  $-3$  to  $+8$   $g$  normal acceleration and  $\pm 1$   $g$  in both the longitudinal and lateral axes. The second package was the dynamic or fine accelerometer system, which covered a smaller acceleration range for better resolution. This range was  $-1$  to  $+3$   $g$  normal acceleration and  $\pm 0.6$   $g$  in both the longitudinal and lateral axes. Both systems measured the aircraft c.g. acceleration in the aircraft body-axis system, but, because they were not precisely located at the c.g., corrections had to be made to the measured data. Accelerometers located away from the c.g. sense angular rates and accelerations that would not be measured at the aircraft c.g. This necessitates including a rate gyro instrumentation package to measure these angular rates and accelerations and correct the sensed accelerations to purely linear c.g. accelerations. Each accelerometer system had its own set of rate gyros and angular accelerometers for this correction. In addition, once corrected to the aircraft c.g., the body-computed accelerations were transformed to the aircraft wind-axis accelerations by using noseboom-measured angle of attack and angle of sideslip. True angle of attack was computed by correcting the measured angle of attack for upwash, sensed pitch, noseboom bending, fuselage bending, and misalignment errors.

### In-flight Thrust Calculation Procedure

The test day in-flight thrust calculation method used was the G.E. F404 gas generator technique, developed for the F404 engine to give accurate engine airflow and thrust over the flight envelope. The in-flight thrust program model was developed from an extensive six-engine test program at the Naval Air Propulsion Center altitude test facility where more than 1500 test points were gathered over the entire engine operating envelope. This extensive database,

combined with sea level static tests, produced an accurate modeling of the engine gas generator, afterburner, and nozzle over the operating envelope.

The thrust calculation method relies on modeling the engine gas generator from which mass flow, temperature, and pressure at the nozzle are computed. The basic approach of the gas generator method is to combine a set of in-flight-measured engine parameters with the engine model. The measured parameters are used where measurements are more accurate than the engine model. An in-flight thrust calculation flow chart is shown in figure 11. This gas generator ideal gross thrust is calculated based on the assumption of a fully expanded nozzle, and it is then corrected for the actual nozzle performance by the nozzle gross thrust coefficient ( $C_{FG}$ ). The calculation procedure can calculate the ideal gross thrust from either the pressure (nozzle throat)-area method or the airflow (nozzle throat)-total temperature method. The pressure-area method is sensitive to an accurate measurement of the nozzle throat area, whereas the airflow-temperature technique relies on an accurate exhaust gas temperature measurement, exhaust mass flow, and an accurate afterburner efficiency model.

The X-29A inlet model uses a wind tunnel-derived inlet pressure recovery factor, Mach and altitude to calculate inlet conditions, and airflow to the engine compressor face. From that point, an energy rise (temperature and pressure) is computed across the fan and high-pressure compressor sections to obtain combustor inlet airflow, temperature, and specific total enthalpy. The combustor and afterburner are modeled separately using an energy balance. The nozzle model is then used to calculate nozzle gross thrust (FG) coefficient from which ideal gross thrust (FGI) is corrected to actual FG. Calculated ram drag (FR), estimated inlet spillage, and nozzle drag components are applied to FG to obtain net thrust (FN). A more detailed discussion of the model and calculation procedure is given in Rooney and Wilt (1985).

A lack of afterburner fuel flow measurement, coupled with a single-point turbine exhaust pressure measurement, resulted in estimated uninstalled thrust accuracy levels of from 5 to 8 percent, depending on flight condition. The computed thrust to obtain a reliable measure of parasite drag ( $C_{Dmin}$ ) is not accurate enough. This deficiency had less effect on determining drag polar shapes. The engine was also not thrust-calibrated, which would have improved the accuracy of the existing instrumentation system. The afterburner fuel measurement deficiency would not allow supersonic drag polar measurement.

### Noseboom Angle-of-Attack Calibration

The noseboom angle-of-attack calibration had more uncertainty than desired. The noseboom system was a modified F-14 flight test system. For the most part, the constant pitch attitude method from a 1-g stabilized flight condition was used to obtain data. Another test technique was a flightpath reconstruction technique (Whitmore, 1985) using data from radar-tracked pushover-pullups and windup turns. Both methods gave inconclusive results due to an unusually large data scatter and a larger-than-normal apparent data bias. The aircraft was difficult to stabilize at a zero pitch rate, which made obtaining calibration data from a 1-g stabilized flight condition very uncertain. In addition, the noseboom exhibited several unusual characteristics such as a resonant vibration with the airframe, which, even with 40-Hz antialiasing filters, caused the data to be very noisy. Random step changes in the angles of attack ( $\alpha$ ) and sideslip ( $\beta$ ) of up to  $\pm 0.5^\circ$  were also seen while flying at the stabilized condition. There appeared to be some type of local flow condition, shock wave interaction, or other local flow perturbations that complicated the effort to obtain a good calibration.

An unexplained angle-of-attack bias of up to  $1^\circ$  developed in the upwash calibration data from both calibration methods, although the indicated bias error was not consistent. Normally, flight test noseboom angle-of-attack calibrations are accurate to better than  $\pm 0.25^\circ$  and the system does not suffer from such large biases in the upwash calibration. Noseboom misalignment, vane calibration, vane or noseboom damage were all checked with no significant results to help understand the problem. Evidence indicates the pitch attitude measurement was not reliable enough and the instrument resolution was inadequate, but this was not conclusively proven to be a significant contributing factor. Analysis of the flightpath acceleration for stabilized turns at Mach 0.90 at 20,000 and 30,000 ft

was performed to compare the results derived from the accelerometer method with that of the energy height method (fig. 12). The accelerometer method uses angle of attack in obtaining aircraft acceleration along the flightpath, whereas the energy height method uses airspeed and altitude only and is, thus, independent of  $\alpha$  measurements. As the energy height method shows, flightpath acceleration in a stabilized turn should be zero, which is in agreement with the accelerometer results using zero  $\alpha$  upwash bias. This supports the conclusion that the noseboom upwash bias was approximately zero. With no evidence to support the existence of an actual bias, a zero bias error in the  $\alpha$  upwash correction was used in the drag polar data reduction.

A drag polar sensitivity analysis was made to determine the impact of this  $\alpha$  uncertainty on drag polars. A more complete sensitivity study of factors affecting drag polar modeling can be found in Powers (1985). The bias error is introduced into the drag polar data through the  $\alpha$  and  $\beta$  transformation of the body-axis accelerations to the aircraft wind axis and in computing thrust components to lift and drag. The effect can be seen in figure 13, which shows a sensitivity of up to 200 drag counts, particularly affecting drag polar shape, but also absolute drag levels. The inclusion of the  $1^\circ$  bias moves the flight test polar results closer to the wind tunnel predictions.

The decision was made at the end of the X-29 flight envelope expansion phase to replace the noseboom with a standard NACA flight test noseboom and recalibrate the system rather than try to continue flying with the original noseboom. This should help since the NACA noseboom is a well-proven system with known characteristics.

## Drag Correction Procedure

**Aerodynamic Drag Corrections.** A drag correction procedure was developed by the aircraft manufacturer and incorporated into the UFTAS performance analysis program. The purpose of this subroutine was to correct the flight test drag data to power-off trimmed flight with the control surfaces in the ACC-schedule configuration for comparison with wind tunnel-generated drag polar predictions. The procedure assumed small perturbation, linear aerodynamic corrections about the trimmed-aircraft configuration. Thus, the method was developed to provide trim drag corrections for control surface configurations that were no more than  $\pm 5^\circ$  off the ACC schedule and for angles of attack that were no more than  $\pm 2^\circ$  from the ACC trim schedule.

The trim drag correction procedure could not be used on some flight data because of the large trim drag errors. These came from large control surface deviations from the ACC trim schedule during highly dynamic maneuvers. Figure 14 shows an example of the large control surface changes from the ACC schedule. In these cases, a drag prediction program estimated the off-ACC schedule dynamic drag levels from the wind tunnel-derived database. The program used flight test time histories of flight conditions, angle of attack, c.g., and actual control surface positions to query the aerodynamic database for the polar and lift curves. In this way, untrimmed flight results could be compared to the wind tunnel predictions where needed.

**Propulsion Drag Corrections.** Other drag data corrections included propulsive drag adjustments to the test day-computed gross thrust. These included ram drag corrections based on engine airflow adjusted by a wind tunnel-derived inlet pressure recovery factor. Data for this inlet recovery factor (fig. 15) were limited because of a limited wind tunnel test and a simplified, flow-through inlet model. The inlet spillage drag (fig. 16) and nozzle drag (fig. 17) component corrections to the test day gross thrust were not based on wind tunnel model tests but were simply estimated, based on results from similar fighter-type aircraft and similar inlet configurations. The component estimates were considered typical of this class of aircraft and constituted at most some 2 to 3 percent of the total gross thrust. Other polar data adjustments included corrections for the thrust moment and trim drag adjustments for off-reference c.g.

## Drag Polar Shape Comparison Methods

**Trimmed and Untrimmed Prediction Comparisons.** Because of the problems associated with the off-ACC schedule maneuver dynamics effects, it was difficult to correct the flight drag polars to the trimmed condition or to compare these polars with the wind tunnel-predicted ACC-trimmed polar shapes. In most cases, the flight test drag polars were not trim-drag corrected. A number of approaches were taken to gain a more complete understanding of the overall performance of the FSW aerodynamics. These included comparing the polar shapes with both the predicted ACC optimum-trimmed polars and the wind tunnel-predicted untrimmed polars. The limitation of a comparison of flight untrimmed polars with wind tunnel-predicted untrimmed polars is that only a single maneuver can be compared since the level of maneuver dynamics from maneuver to maneuver will vary. The polar shape differences may not be totally due to aerodynamics but, rather, due in part to errors in predicted maneuver dynamics. The untrimmed aerodynamic performance comparison could also not represent the best performance the aircraft was supposed to achieve with the optimum ACC trim schedule at a given coefficient of lift. For completeness, the flight untrimmed polars were compared with both predicted ACC trimmed and dynamic untrimmed polar shapes. Comparison with the predicted untrimmed polars gave the basic wind tunnel-to-flight test correlation and a comparison with the ACC trimmed polar determined how well the untrimmed flight aerodynamic performed against the so-called optimum lift-to-drag performance of the ACC schedule configuration.

**Comparison Methods With Other Aircraft.** Another analytical method of comparing drag polar shapes was undertaken to obtain a measure of the aerodynamic performance improvements of the FSW in comparison with acknowledged modern ASW fighter designs. Several analytical approaches are possible when comparing aircraft drag polars with other aircraft. Two techniques are to compare the absolute polars using the reference area or the span-squared method. The technique used here is based on the classical Prandtl method of comparing the induced drag polar shapes by subtracting the in-flight-measured  $C_{Dmin}$  value from the drag level of each respective aircraft. All comparison aircraft-induced drag levels are then corrected to the X-29A reference aspect ratio of 4.0. For a given coefficient of lift range, the polar shapes are then primarily a function of the overall aircraft configuration Oswald aerodynamic efficiency factor. The Prandtl method relies on the assumption that angle of attack is less than  $20^\circ$  and that all aircraft basic aspect ratios are greater than or equal to 3.0. The X-29A and the comparison aircraft fulfill this requirement. Details of the technique can be found in numerous aerodynamics textbooks such as Clancy (1975).

## RESULTS AND DISCUSSION

### Aircraft Configuration Changes

The X-29A external aircraft configuration was not constant during the course of the flight envelope expansion program. The changes, summarized in table 3, included the addition of the FDMS and the flaperon structural excitation system. In an effort to keep track of all external aircraft configuration changes affecting aerodynamics, dynamic pushover-pullups and windup turns were flown to measure the drag polar changes. These effects, though small, are evaluated in figures 18 to 21.

To assist with the structural loads clearance and the in-flight monitoring of wing deflections, the FDMS was installed on the upper surface of the right wing beginning with flight 9. This system added a protuberance drag component to the wing as well as probably increasing the overall parasite drag by increasing wing skin friction drag from localized increases in turbulence. An attempt was made to measure this drag component with the limited accuracy of the thrust measurement system. Results shown in figure 18 indicate an increased drag increment of as much as 50 to 60 drag counts, but this is inconclusive because of the uncertainty in  $C_{Dmin}$  values obtained from thrust calculations.

To aid in flow visualization tests, tufts and flow cones were added during flights 12, 13, and 16. These devices were small and did not have a measurable effect on the aircraft drag.

Beginning with flight 19, the flaperon shaker excitation system was added on each wing mid- and outboard flaperon at the aft end of the outboard flaperon actuator housing. A modified shaker fairing was necessary in order to enclose the shaker (fig. 19). It was suspected that this could increase the base drag behind the wing, and attempts to measure the drag increment can be seen in figure 20. The polar shows an effect on the drag level above a  $C_L$  of 1.20, but again uncertainties in the thrust-derived  $C_{Dmin}$  values made this inconclusive.

An FCS software modification beginning with flight 23 changed the ACC scheduling of the canards and strake flaps in an attempt to correct for a saturated, full-down flaperon effect on the integration of the strake flap position. The integration of the strake flap position with flaperons fully down was to keep the canards on their trim schedule, but the integration logic did not work properly when the flaperons were being used for aileron control. The FCS computers subsequently failed to recognize a full-down flaperon condition. A software change corrected the problem by allowing the FCS computers to recognize the fully-down flaperons as saturated even with aileron inputs. Figure 21 shows the changes in the drag polar above a  $C_L$  of 1.20 as a result of this trim schedule change. The change affected the overall trimmed ACC schedule tracking of the canard and strake flaps during maneuvers and resulted in slightly improved aircraft performance.

## Drag Polar Results

Figures 22 to 27 show the results of the subsonic X-29 drag polars in comparison with both untrimmed and ACC-trimmed drag polar predictions. Results demonstrate that the polar shapes met or exceeded predictions. Data are shown primarily at an altitude of 40,000 ft with some additional data for Mach 0.60 at only 30,000 ft. The Mach 0.90 polar is shown at both 30,000 and 40,000 ft, where the 30,000-ft design condition only reaches a maximum  $C_L$  of 1.10 and is shown in comparison with the 40,000-ft results. The polar shapes were studied as a function of Mach number and angle of attack only. Such effects as dynamic pressure and Reynolds number or skin friction drag on the drag polars were not evaluated for this initial flight envelope expansion phase. Polar data was limited in angle of attack by structural loads and aerodynamic buffet considerations. Data were primarily obtained from Mach 0.60 to Mach 0.95 at angles of attack up to  $15^\circ$  at the lower subsonic region and up to  $12$  to  $13^\circ$  in the transonic region. Flight test data scatter was  $\pm 5$  percent for each polar, which was considered nominal flight quality and sufficient for a preliminary assessment of polar shape.

Figure 22 shows the drag polar and lift curve  $C_L - \alpha$  results at Mach 0.60, 30,000 ft. In the drag polar (fig. 22(a)), the flight data are 15 to 20 percent lower in drag over the entire angle-of-attack range than the polars predicted, based on the trimmed ACC schedule and the untrimmed dynamics. The lift curve in fig. 22(b) shows the same improvements over predicted data and shows the change in lift curve slope at the same  $C_L$  of 1.10, as predicted. Note that the maneuver dynamics effects on the polar are negligible, as seen in the agreement between the predicted ACC schedule and the dynamic flight results. This is due to the slow (30 sec) maneuver rate of the windup turn. Using the  $C_L^2$  as a function of  $C_D$  form of the polar (fig. 22(c)), the data lose linear behavior above a  $C_L$  of 0.95. This was found to be true over the Mach number range. The Oswald aerodynamic efficiency factor and the lift-to-drag ratio (L/D) at the design  $C_L$  of 0.92 were determined to be 74 percent and 8.36, respectively. This is better than the predicted 70 percent efficiency factor and an L/D of 7.13. Table 4 shows summarized results of aerodynamic efficiency factors and L/D for each Mach number compared with the predicted ACC schedule and the predicted dynamic condition.

Figure 23 shows the drag polar and lift curve for Mach 0.70 at 40,000 ft. As shown in figure 23(a), drag improvements over predicted results are still approximately 15 to 20 percent, particularly above a  $C_L$  of 0.80. The effects of higher dynamic maneuver rates (10 sec) can be seen in the difference between the two predicted polar fairings (fig. 23(a)) and in the lift curve predictions (fig. 23(b)). Figure 23(b) also shows the maneuver dynamic effects on

the measured flight data with a large variation in  $C_L$  for a given angle of attack. These data were generated from a rapid pushover-pullup maneuver. The apparent hysteresis band is due to the control surfaces being at different positions (up to  $4^\circ$  difference for the canards and up to  $9^\circ$  difference for the flaperons) as a given angle of attack is attained during different phases of the maneuver. The efficiency factor and L/D for Mach 0.70 (fig. 23(c)) were 72 percent and 7.67, respectively.

Figures 24 and 25 show the drag polar and lift curve for Mach 0.80 and 0.85, respectively, at 40,000 ft. The lower-than-predicted drag level difference for both Mach polars (figs. 24(a) and 25(a)) decreased to approximately 10 to 12 percent above a  $C_L$  of 0.80 as the aircraft approached the transonic drag rise. Below a  $C_L$  of 0.80, the flight data agreed with predictions. Again, differences between the predicted ACC-trimmed and dynamic untrimmed curves can be attributed to maneuver dynamics effects. The corresponding lift curves are shown in figures 24(b) and 25(b). Figures 24(c) and 25(c) were used to extract the respective efficiency factors and lift-to-drag ratios. For Mach 0.80, these were 72 percent and 7.48, respectively, compared with 70 percent and 7.19 for Mach 0.85.

Figure 26 shows the transonic drag polar and lift curve for Mach 0.90. The Mach 0.90/30,000-ft design condition flight data are shown along with the Mach 0.90/40,000-ft data in the drag polar of figure 26(a). The Mach 0.90 lift curve (fig. 26(b)) contains only 40,000-ft flight data. At both Mach conditions, the flight drag data are approximately 5 to 7 percent better than predicted above a  $C_L$  of 0.80. Below this coefficient of lift, the flight results agree well with predictions. The lift curve results of figure 26(b) show a similar trend above a  $7^\circ$  angle of attack. The Oswald efficiency factor and L/D, as extracted from figure 26(c) at the design  $C_L$  of 0.92, were 63 percent and 6.53, respectively, and are slightly better than the predicted ACC values of 59 percent and 6.27.

Figure 27 shows the Mach 0.95, 40,000-ft comparison between flight results and predictions. In figure 27(a), the polar results are 5 percent better than predicted above a  $C_L$  of 0.90. Below this  $C_L$ , the flight data have increasingly more drag than predicted up to 20 percent as coefficient of lift decreases to zero. Although the lift curve results are not as clearly defined, the data (fig. 27(b)) show the same type of trend above an angle of attack of  $7^\circ$ . The aerodynamic efficiency factor and L/D were 63 percent and 6.46, respectively.

A more accurate calculation of  $C_{D_{min}}$  is required to completely analyze the polar shapes relative to predictions. Where maneuver dynamic effects were large enough, the dynamic untrimmed predicted polars consistently showed a higher drag level than the more optimum-trimmed ACC-schedule-predicted polars. Areas where the difference between ACC and dynamic predictions were significant occurred during the more dynamic windup turn maneuvers. Windup turn maneuvers are in general more dynamic in nature than the pushover-pullup maneuvers that were used to generate the mid- to lower-range polar data. This shows at  $C_L$ s above 0.90, where the windup turn maneuver generated all the flight polar data. Further testing and analysis, with the calibrated engine installed, needs to be done to fully understand the flight-to-predicted differences.

Figure 28 shows the results of comparing the X-29A Mach 0.60 drag polar shape against a band of several modern-day fighter aircraft flight test-derived polars at the same Mach number. The X-29A predicted polar shape for Mach 0.6 is also presented for comparison with the flight results. It should be noted that the X-29A flight test results have not been trim-drag corrected. The figure gives a measure of the aeroperformance potential of the X-29A FSW configuration. This is not the total story of potential aircraft performance advantages, since such things as wing loading and thrust-to-weight ratio also play a decisive role in the ultimate performance potential of an aircraft. To derive an aerodynamic efficiency factor, the slope was taken between a  $C_L$  of 0 and 1.0. The respective efficiency factors in this range do not represent any mission design  $C_L$  of any of the comparison aircraft, including the X-29A. It was simply a convenient place to take a useful slope and is a typical coefficient of lift range at which fighter-type aircraft maneuver. At Mach 0.60, X-29A flight results yielded an Oswald efficiency factor of 74 percent compared with a predicted value of 70 percent. The aircraft band at this  $C_L$  range had corresponding values of 34 to 52 percent.

## FUTURE WORK

Future performance and propulsion work include more precise drag measurements over the entire flight envelope and drag polar modeling at supersonic Mach numbers. More detailed performance and drag measurements will be possible because of the installation of a thrust-calibrated F404 engine. A more detailed analysis will be made to better understand the differences between flight and prediction results and to correlate the pressure distribution measurements with the accelerometer-measured aeroperformance. An effort will be made to evaluate the separate aerodynamic performance of the wing and canard and to analyze the wing/canard aerodynamic interaction. In addition, more emphasis will be focussed on obtaining point performance data, especially at the Mach 0.9 and Mach 1.2 design points at 30,000 ft. This will include thrust-limited turning performance and energy maneuverability analysis.

## CONCLUSIONS

A preliminary investigation of the subsonic lift and drag characteristics of the X-29A aircraft was conducted and compared with predictions. It was found that the performance flight test results in the subsonic flight envelope were equal to or better than predictions over the Mach number range to 0.95 and up to 15° angle of attack. This was especially true at coefficients of lift above 0.90 for the induced drag polar shapes. The absolute drag level and polar shape compared slightly better than predictions at the subsonic design point of Mach 0.90. Drag data was consistent within itself and exhibits a typical data scatter of  $\pm 5$  percent. The drag polar results were not trim-drag-corrected and contain maneuver dynamic effects due to being significantly off the ACC control surface trim schedule. The trim drag correction procedure developed to correct for these dynamics and other effects was unable to correct for such large off-schedule effects. Angle-of-attack calibration on the X-29A was particularly difficult, especially with the upwash correction. Limited flight data indicate that the apparent upwash bias was zero. The apparent  $\alpha$  calibration uncertainty could have an effect on drag polar data of up to 200 drag counts and can affect the assessment of the aircraft aeroperformance drag polar shapes. Further analysis needs to be done to fully understand the difference between predicted and flight results.

*Ames Research Center  
Dryden Flight Research Facility  
National Aeronautics and Space Administration  
Edwards, California, February 5, 1988*

## REFERENCES

- Air Force Flight Test Center, *Documentation of the Uniform Flight Test Analysis System (UFTAS)*, Edwards A.F.B., Calif., June 1973, vols. 1 and 2.
- Bowers, Albion H., *X-29A Longitudinal and Directional Force and Moment Supplemental Transonic Wind Tunnel Test Results*, NASA TM-85909, 1984 (FEDD).
- Charletta, R., *Series I Transonic/Supersonic Testing on a 12.5% Scale Grumman Design 712, X-29A Forward-Swept Wing Demonstrator Model in the NASA-ARC 11 Foot and 9 × 7 Foot Wind Tunnels at Moffett Field, Calif.*, AER/T-Ames-538-1-11, 97, vols. 1-3, Grumman Aerosp. Corp., Bethpage, NY, 1982.
- Clancy, L.J., *Aerodynamics*, John Wiley and Sons, New York, 1975.
- Hicks, John W., James M. Cooper, Jr., and Walter J. Sefic, *Flight Test Techniques for the X-29A Aircraft*, AIAA 87-0082, Jan. 1987.
- Hicks, John W. and Neil W. Matheny, *Preliminary Flight Test Assessment of the X-29A Advanced Technology Demonstrator*, AIAA 87-2949, Sept. 1987.
- Krone, N.J., Jr., *Divergence Elimination With Advanced Composites*, AIAA 75-1009, Aug. 1975.
- Powers, S.G., *Predicted X-29A Lift and Drag Coefficient Uncertainties Caused by Errors in Selected Parameters*, NASA TM-86747, 1985.
- Rooney, E.C. and C.E. Wilt, *Development of In-flight Thrust Measurement Procedures for Afterburning Turbofan Engine*, AIAA 85-1405, July 1985.
- Sefic, Walter J. and William Cutler, *X-29A Advanced Technology Demonstrator Program Overview*, AIAA 86-9727, April 1986.
- Whitmore, Stephen A., *Formulation and Implementation of Nonstationary Adaptive Estimation Algorithm With Application to Air-Data Reconstruction*, NASA TM-86727, 1985.

## APPENDIX — DATA REDUCTION

To compute aircraft performance or drag polars using the body-mounted accelerometer system, the first step in the data reduction process was to correct the linear accelerometer measurements for sensed angular velocities and accelerations not being experienced by the aircraft c.g. These non-c.g. motions are sensed when the accelerometer instrumentation is located away from the c.g. in the airframe. For an instrumentation package located at the c.g., these angular velocities and accelerations about the c.g. would be identically zero. Once the measured accelerations were corrected to the aircraft c.g., the second step was to transform or correct those body-axis-sensed accelerations to the aircraft wind-axis system. Drag polar and other aircraft performance are measured in the wind-axis system. The transformation was accomplished through the aircraft angles of attack and sideslip.

The angular corrections of the accelerometers to the aircraft c.g. are

$$n_{xb} = n_{xm} + \Delta n_x, n_{yb} = n_{ym} + \Delta n_y, n_{zb} = n_{zm} + \Delta n_z, \quad (1)$$

and

$$\begin{aligned} \Delta n_x &= 1/g(\dot{r}I_y - \dot{q}I_z + (q^2 + r^2)I_x - pqI_y - prI_r) \\ \Delta n_y &= 1/g(\dot{p}I_z - \dot{r}I_x + (p^2 + r^2)I_y - rqI_z - pqI_x) \\ \Delta n_z &= 1/g(\dot{q}I_x - \dot{p}I_y + (p^2 + q^2)I_z - prI_x - rqI_y) \end{aligned} \quad (2)$$

where

- $n_{xm}$  = measured longitudinal acceleration
- $n_{ym}$  = measured lateral acceleration
- $n_{zm}$  = measured vertical or normal acceleration
- $n_{xb}$  = body-axis c.g. longitudinal acceleration
- $n_{yb}$  = body-axis c.g. lateral acceleration
- $n_{zb}$  = body-axis c.g. vertical or normal acceleration
- $\Delta n_x$  = body-axis longitudinal accelerometer angular rate correction
- $\Delta n_y$  = body-axis lateral accelerometer angular rate correction
- $\Delta n_z$  = body-axis normal accelerometer angular rate correction
- $I_x$  = longitudinal displacement of the accelerometer from the aircraft c.g.
- $I_y$  = lateral displacement of the accelerometer from the aircraft c.g.
- $I_z$  = vertical displacement of the accelerometer from the aircraft c.g.
- $g$  = earth acceleration
- $p$  = aircraft roll rate
- $q$  = aircraft pitch rate
- $r$  = aircraft yaw rate
- $\dot{p}$  = aircraft roll acceleration
- $\dot{q}$  = aircraft pitch acceleration
- $\dot{r}$  = aircraft yaw acceleration

Note that it is necessary that the angular velocity and acceleration sensors be collocated with the linear accelerometers.

In order to transform the body-axis c.g. acceleration measurements to the aircraft wind-axis system, the noseboom true angle of attack had to be calculated. For performance tests, maneuvers were flown at essentially zero sideslip  $\beta$ , so only uncorrected measurements of  $\beta$  were used, where small  $\beta$  angles have little effect on the results. Thus,

$$\begin{aligned}\alpha_T &= \alpha_m + \Delta\alpha_u + \Delta\alpha_q + \Delta\alpha_{bb} + \Delta\alpha_{fb} + \Delta\alpha_{mis} \\ \beta_T &= \beta_m\end{aligned}$$

and

$$\Delta\alpha_q = \tan^{-1} [ I_x q \cos \alpha_m / (V_T - I_x q \sin \alpha_m) ] \quad (3)$$

where

- $\alpha_T$  = true angle of attack
- $\alpha_m$  = measured angle of attack
- $\Delta\alpha_u$  = angle-of-attack upwash correction
- $\Delta\alpha_q$  = angle-of-attack pitch rate correction
- $\Delta\alpha_{bb}$  = angle-of-attack noseboom bending correction
- $\Delta\alpha_{fb}$  = angle-of-attack fuselage bending correction
- $\Delta\alpha_{mis}$  = angle-of-attack vane and noseboom misalignment correction
- $\beta_m$  = measured sideslip angle
- $\beta_T$  = true sideslip angle
- $V_T$  = true airspeed

All corrections, except pitch rate correction, are determined from airborne or ground calibrations. A zero upwash correction bias was assumed for  $\Delta\alpha_u$ .

The body-axis accelerations were then transformed to the aircraft wind-axis system by

$$\begin{bmatrix} n_{xw} \\ n_{yw} \\ n_{zw} \end{bmatrix} = \begin{bmatrix} \cos \beta_T & \sin \beta_T & 0 \\ -\sin \beta_T & \cos \beta_T & 0 \\ 0 & 0 & 1 \end{bmatrix} \begin{bmatrix} \cos \alpha_T & 0 & -\sin \alpha_T \\ 0 & 1 & 0 \\ \sin \alpha_T & 0 & \cos \alpha_T \end{bmatrix} \begin{bmatrix} n_{xb} \\ n_{yb} \\ n_{zb} \end{bmatrix} \quad (4)$$

where

- $n_{xw}$  = wind-axis c.g. longitudinal acceleration
- $n_{yw}$  = wind-axis c.g. lateral acceleration
- $n_{zw}$  = wind-axis c.g. normal acceleration

Once the proper wind-axis aircraft c.g. accelerations were computed, this was combined with thrust, gross weight, and dynamic pressure calculations to compute coefficients of lift and drag. Test day gross thrust was computed from the General Electric F404-GE-400 mass flow method. Propulsive drag corrections were applied to the gross thrust to obtain net thrust available, where

$$F_{nt} = F_{gt} - F_{rt} - F_{it} - F_{Nt} \quad (5)$$

and

- $F_{nt}$  = test day net thrust available
- $F_{gt}$  = test day gross thrust
- $F_{rt}$  = test day ram drag, computed from engine airflow
- $F_{it}$  = test day inlet spillage drag
- $F_{Nt}$  = test day nozzle drag

Aircraft excess thrust was computed from

$$F_{ex} = n_{xw}W_t \quad (6)$$

where

- $F_{ex}$  = test day excess thrust
- $W_t$  = aircraft gross weight

Excess thrust was subtracted from net thrust available to yield net thrust required from which the coefficient of drag was computed by

$$C_D = (F_{nt} - F_{ex})/qS \quad (7)$$

Note that  $C_D$  represents an untrimmed drag-corrected value. The coefficient of lift was obtained from

$$C_L = [n_{zw}W_t - F_{gt} \sin(\alpha_T + i)]/qS \quad (8)$$

where

- $i$  = engine-thrust incidence angle, with respect to the airframe (zero for the X-29A)

When the angle of attack and control surface deflection fell within the specified limits, the trim drag corrections were applied to the data to obtain trimmed drag polars. Otherwise, the untrimmed values of  $C_L$  and  $C_D$  were used to compare polar shapes with predictions.

TABLE 1. AIRCRAFT GEOMETRY AND MASS CHARACTERISTICS

Total height, ft	14.29
Total length, ft	48.1
Wing	
Reference planform area, ft <sup>2</sup>	185.0
Reference span, ft	27.2
Reference chord, ft	7.216
Root chord, ft	9.72
Aspect ratio	4.0
Taper ratio	0.4
Airfoil	GAC K-Mod 2 supercritical
Airfoil thickness (root), percent	6.7
Airfoil thickness (tip), percent	4.9
Dihedral angle, deg	0
Twist, deg	7
Root incidence angle, deg	-5
Quarter-chord sweep angle, deg	-33.73
Leading-edge sweep angle, deg	-29.27
Vertical tail	
Area, ft <sup>2</sup>	33.75
Span, ft	5.5
Chord, ft	6.67
Root chord, ft	7.75
Aspect ratio	2.64
Taper ratio	0.306
Airfoil	Symmetrical
Airfoil thickness (root), percent	4.0
Quarter-chord sweep angle, deg	41.05
Leading-edge sweep angle, deg	47.00
Canard	
Planform area, ft <sup>2</sup>	37.00
Span, ft	13.63
Chord, ft	5.46
Root chord, ft	7.61
Aspect ratio	1.47
Taper ratio	0.318
Airfoil	Symmetrical
Airfoil thickness (root), percent	5.0
Airfoil thickness (tip), percent	3.5
Dihedral angle, deg	0
Quarter-chord sweep angle, deg	23.08
Leading-edge sweep angle, deg	42.00
Deflection range, deg	+30 to -60

TABLE 1. CONCLUDED

<b>Wing flap</b>	
Hinge line, percent of wing root chord .....	0.75
Half-span, ft .....	9.35
Area, ft <sup>2</sup> .....	14.32
Root station, percent of wing half-span .....	0.28
Root chord, ft .....	2.43
Hinge-line sweep angle, deg .....	42.0
Deflection range, deg .....	-10 to +25
<b>Strake flap</b>	
Half-span, ft .....	2.08
Area, ft <sup>2</sup> .....	5.21
Root station, percent of strake half-span .....	0
Root chord, ft .....	2.50
Hinge-line sweep angle, deg .....	0
Deflection range, deg .....	±30
<b>Rudder</b>	
Hinge line, percent of vertical stabilizer chord .....	0.70
Span, ft .....	6.67
Area, ft <sup>2</sup> .....	7.31
Root station, percent of vertical stabilizer .....	0.18
Root chord, ft .....	2.33
Hinge-line sweep angle, deg .....	27
Deflection range, deg .....	±30
<b>Masses</b>	
Empty weight, lb .....	13,948
Useful load, lb .....	3882
Fuel load, lb .....	3662
Gross weight, lb .....	17,830
<b>Powerplant</b>	
Engine .....	single General Electric F404-GE-400
Sea level static thrust, lb .....	16,012

TABLE 2. WIND TUNNEL DATABASE

	1979	1980	1982	1983
	J A S O N D	J F M A M J J A S O N D	J F M A M J J A S O	J F M A M J J A
GWTT 368 (high $\alpha$ )	▲ 44 hours			
CALSPAN SI (trans)		▲ 25		
GWTT 372		▲ 216		
AEDC 16T SII (super) (high $\alpha$ )		▲ 50 ▲ 18		
CALSPAN SII (trans)		▲ 85		
GWTT 380 (STOL)		▲ 75		
Ames 12 ft (high $\alpha$ )			▲ 40	
Ames 9 ft x 7 ft (super)			▲ 120	
Ames 11 ft (trans)			▲ 320	▲ 80
GWTT 399 (ground effect)				▲ 295

TABLE 3. AIRCRAFT CONFIGURATION CHANGES

Flight number	FDMS	Flaperon shaker	Tufts	ACC
1	None	None	None	Original
9	Installed	None	None	Original
12	Installed	None	Installed	Original
13	Installed	None	Installed	Original
16	Installed	None	Installed	Original
19	Installed	Installed	None	Original
23 to 104	Installed	Installed	None	Modified

TABLE 4. SUMMARY OF SUBSONIC DRAG POLAR  
OSWALD AERODYNAMIC EFFICIENCY FACTOR  
AND LIFT-TO-DRAG RATIO

Mach number	Aerodynamic efficiency factor	Lift-to-drag ratio
0.60		
Flight data	0.74	8.36
Predicted ACC	0.70	7.13
Predicted dynamic	0.70	7.05
0.70		
Flight data	0.72	7.67
Predicted ACC	0.66	6.84
Predicted dynamic	0.63	6.57
0.80		
Flight data	0.72	7.48
Predicted ACC	0.63	6.64
Predicted dynamic	0.63	6.31
0.85		
Flight data	0.70	7.19
Predicted ACC	0.62	6.44
Predicted dynamic	0.61	6.30
0.90		
Flight data	0.63	6.53
Predicted ACC	0.59	6.27
Predicted dynamic	0.59	6.22
0.95		
Flight data	0.63	6.46
Predicted ACC	0.58	6.29
Predicted dynamic	0.58	5.92

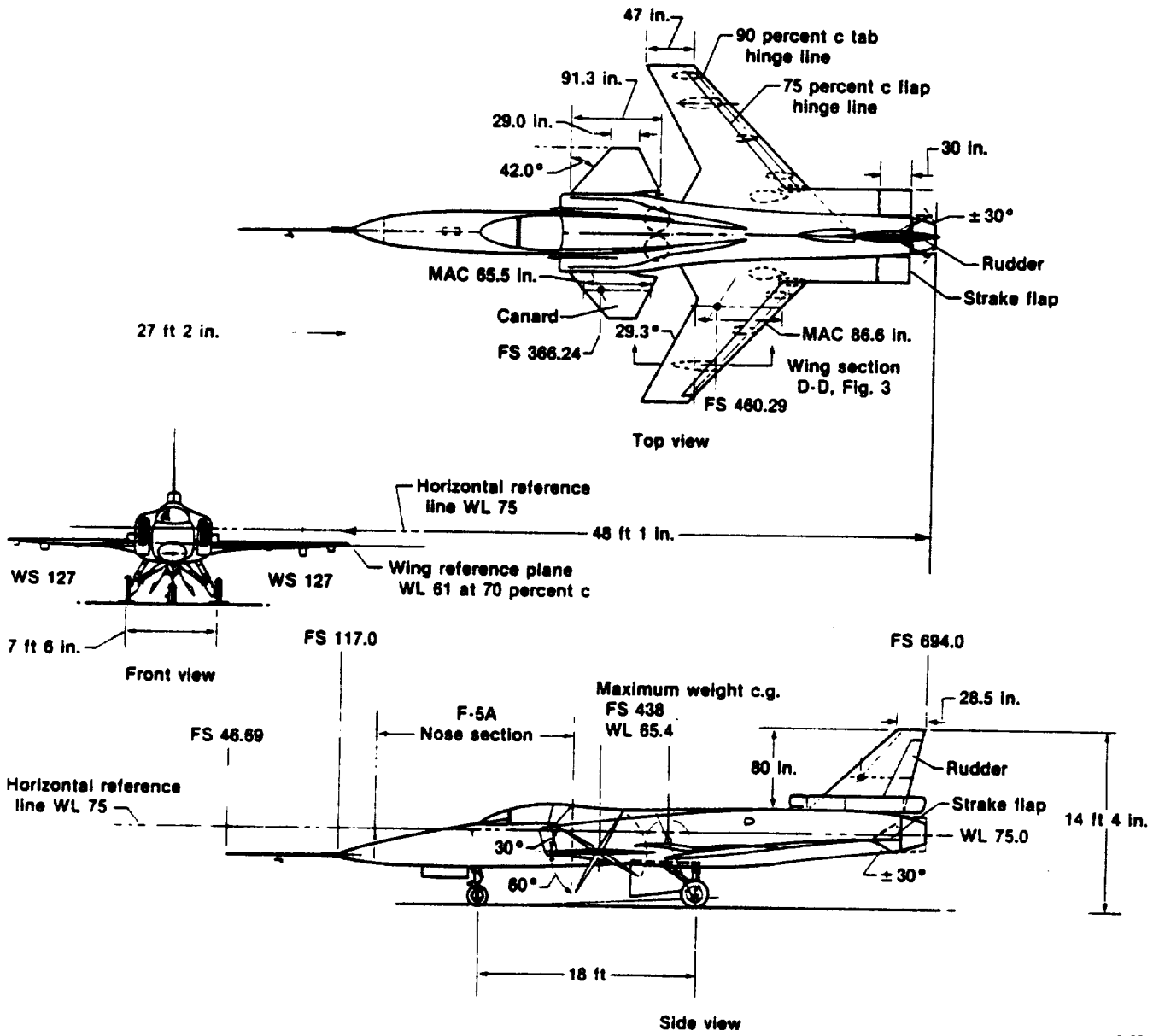
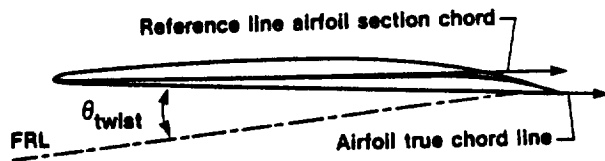
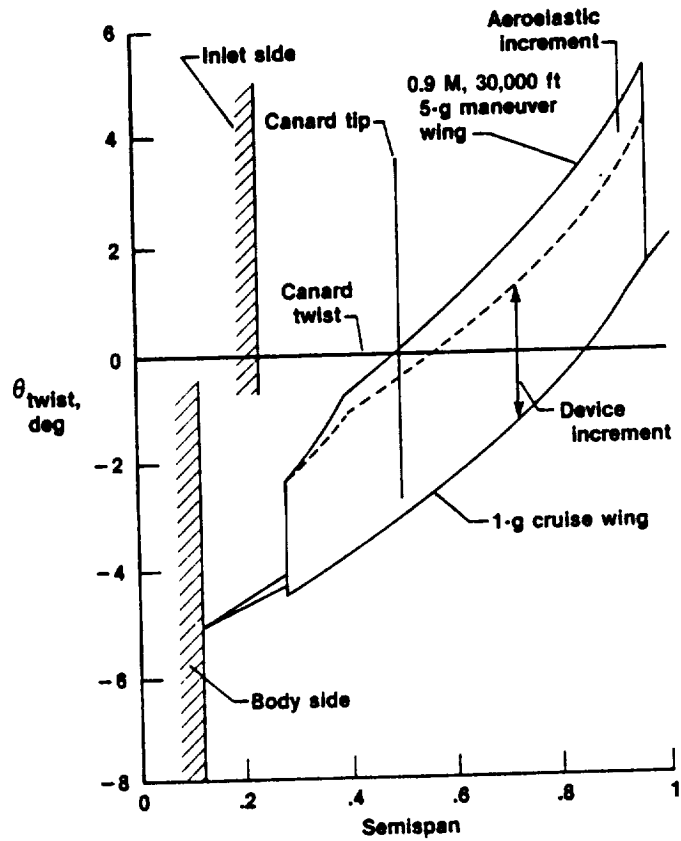


Figure 1. X-29A aircraft.

8437



Note: Twist angle plotted above refers to angle between airfoil true chord-line and fuselage ref line, as shown in sketch at right

8438

Figure 2. Canard and wing twist distribution.

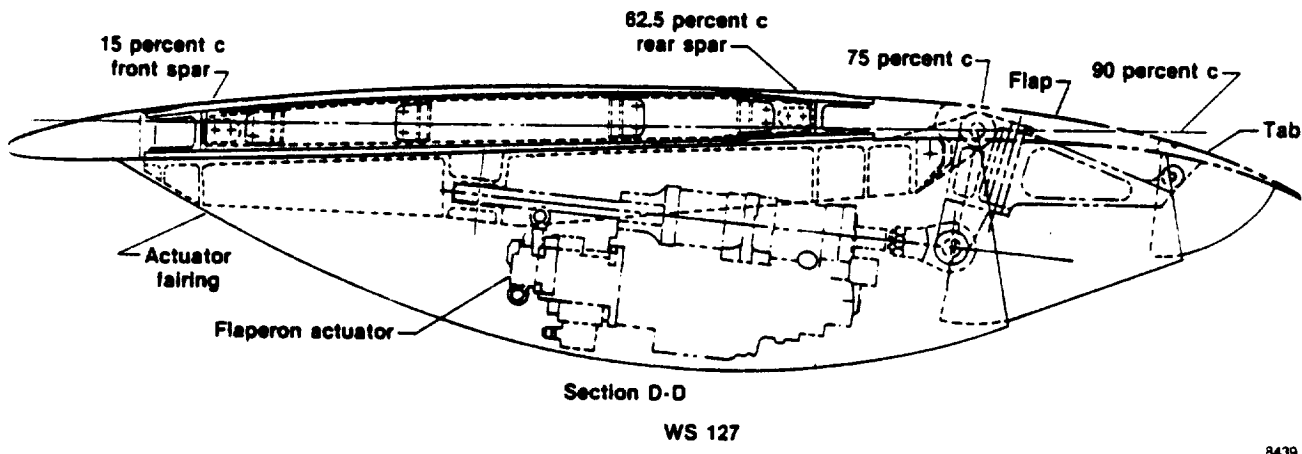


Figure 3. X-29A wing section and flaperon actuator fairing.

8439

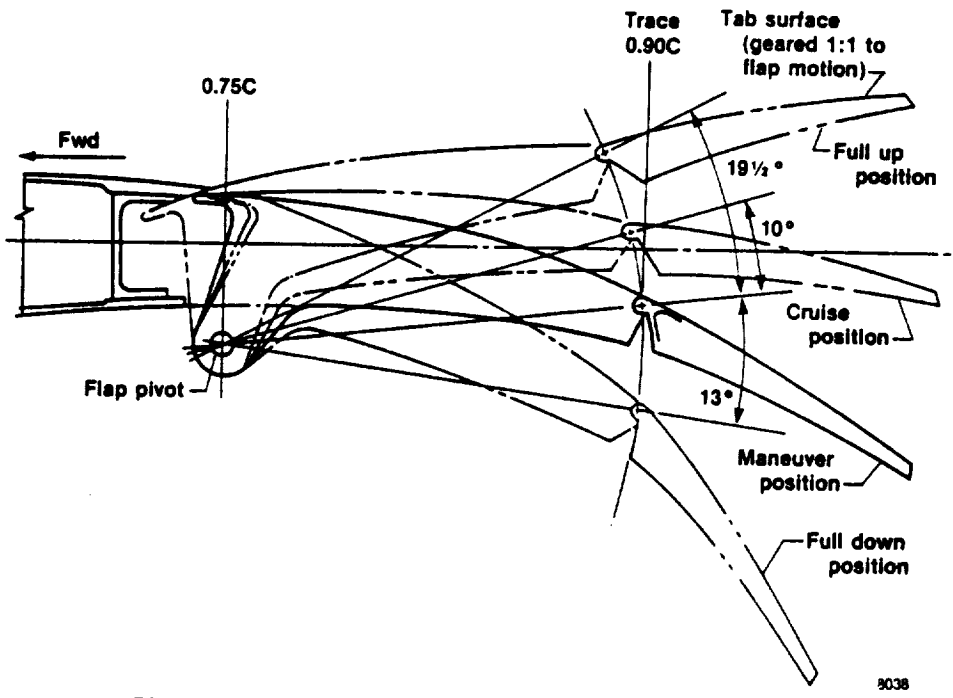
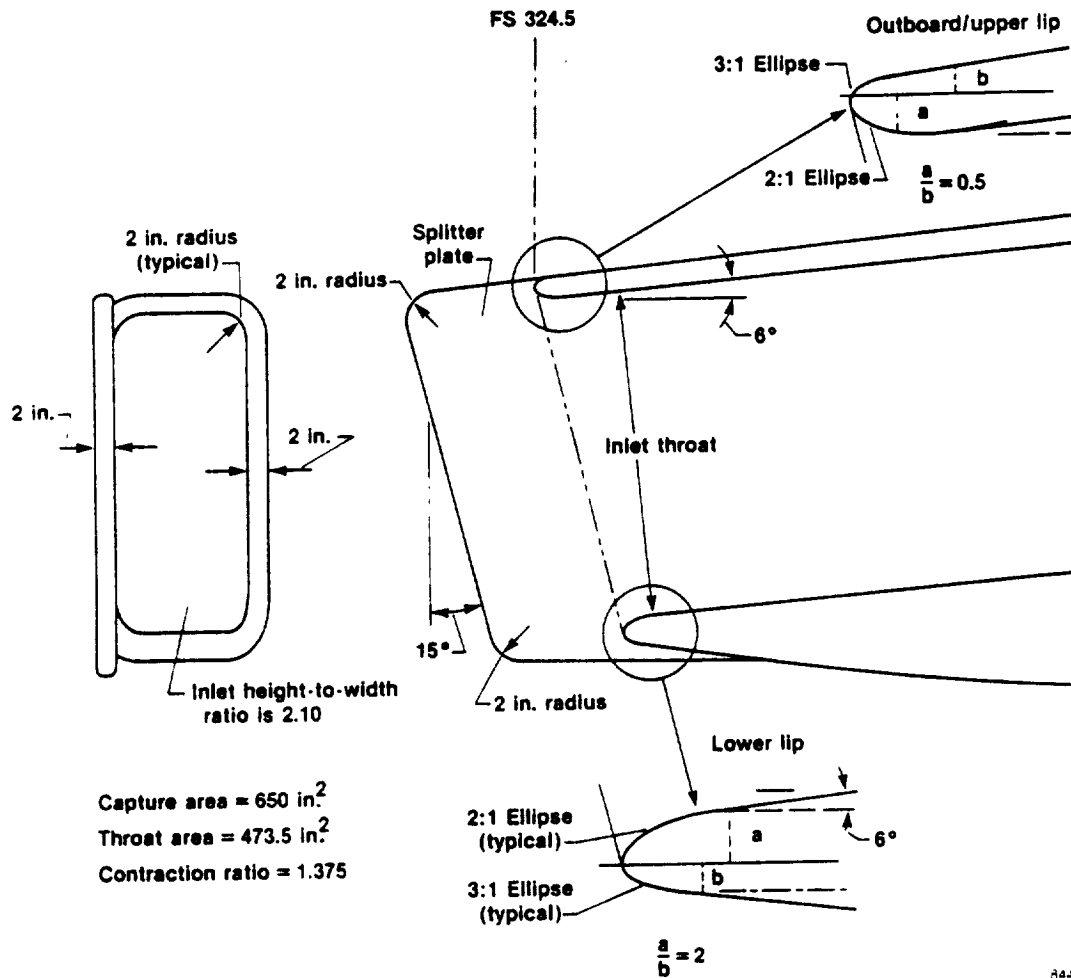


Figure 4. Flap-tab geometry (section normal to 0.75C).

8038



8440

Figure 5. X-29A inlet design.

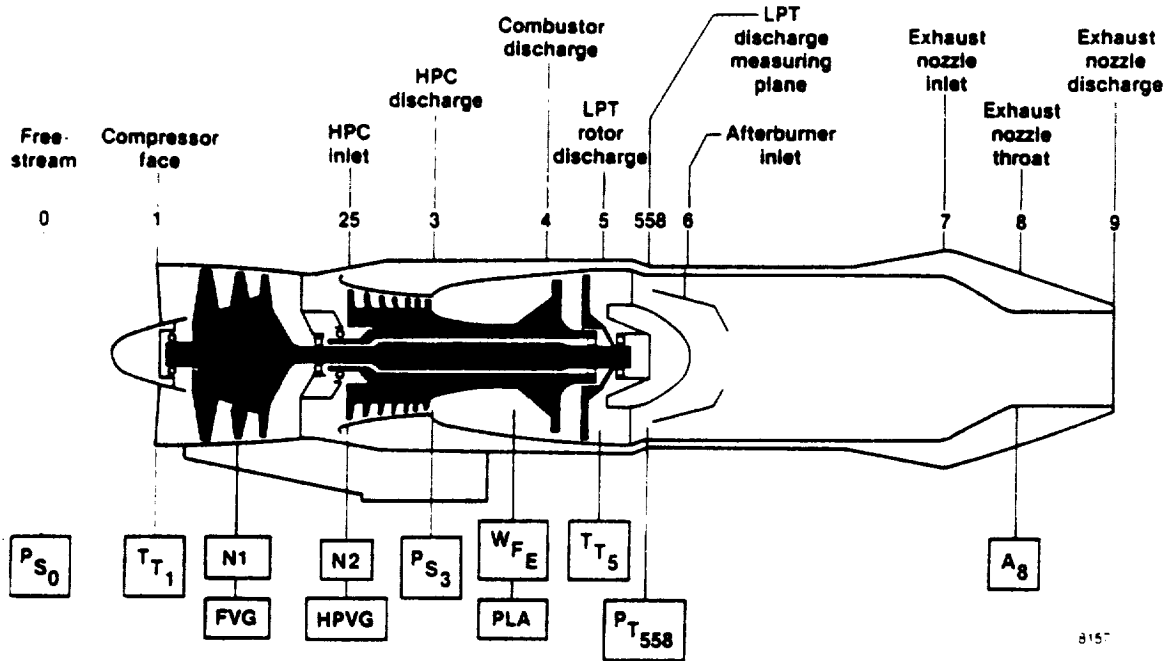


Figure 6. Engine station and sensor locations.

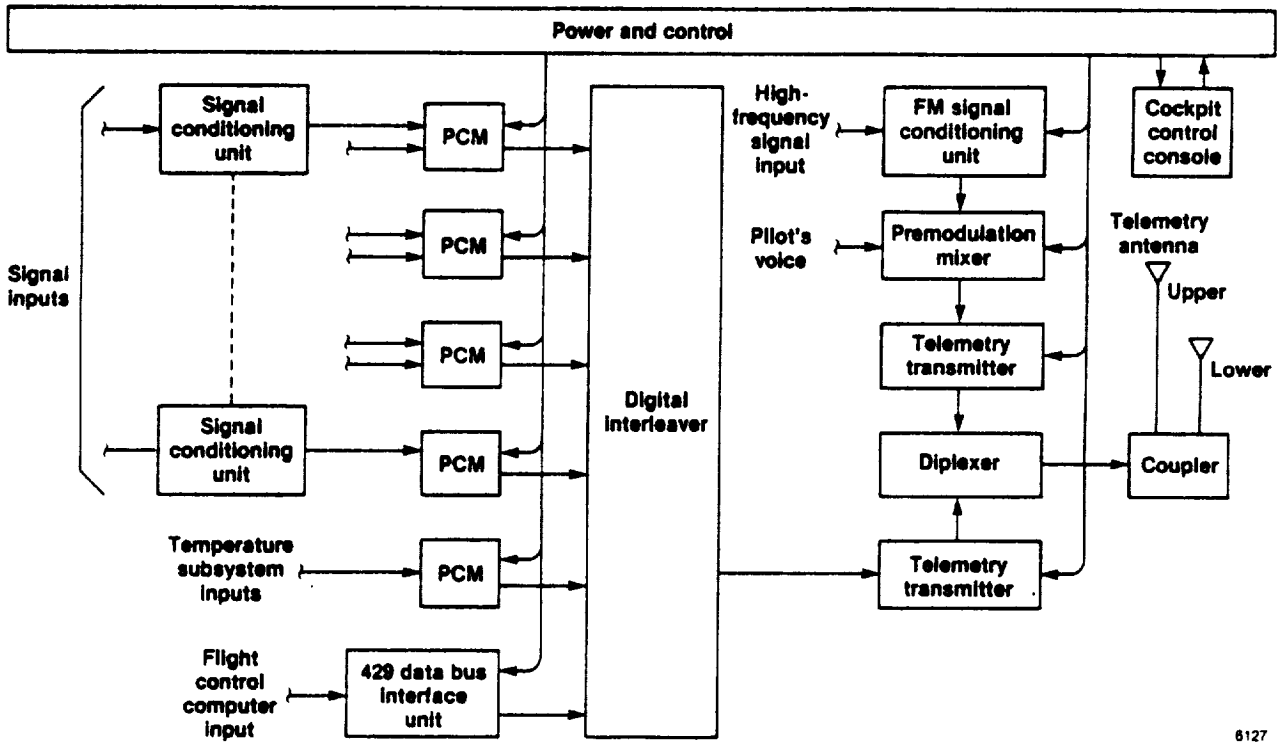


Figure 7. Aircraft instrumentation system.

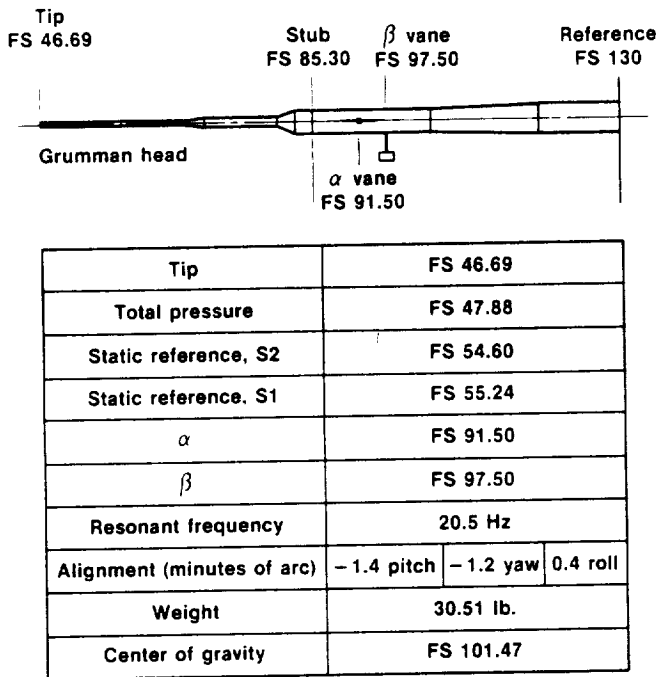
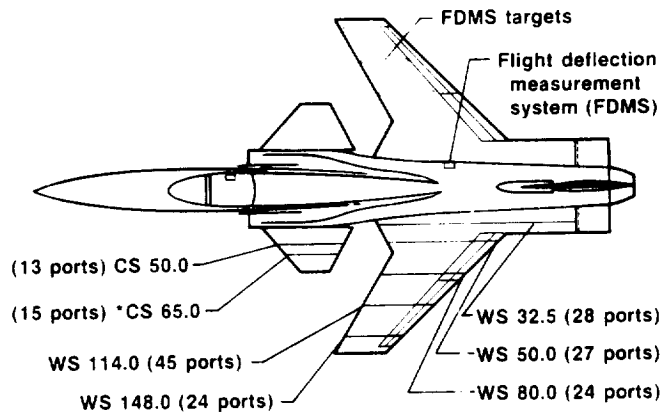


Figure 8. Flight test noseboom.



\*This row was not on wind tunnel model

8443

Figure 9. Static pressure orifice row locations.

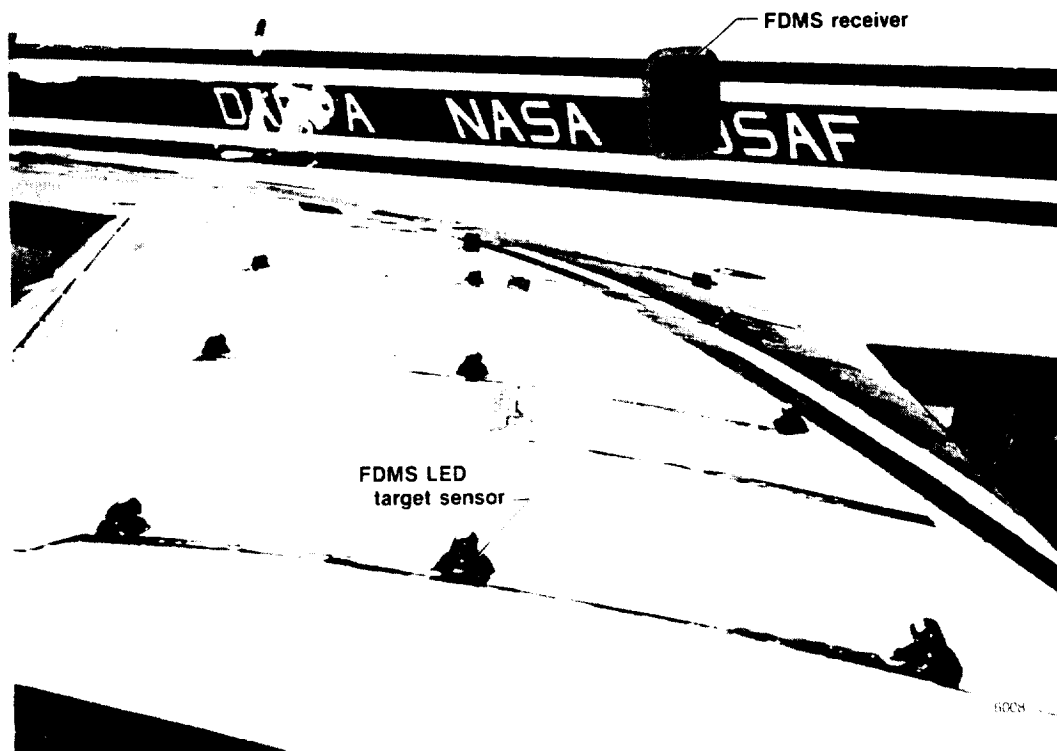


Figure 10. Flight deflection measurement system.

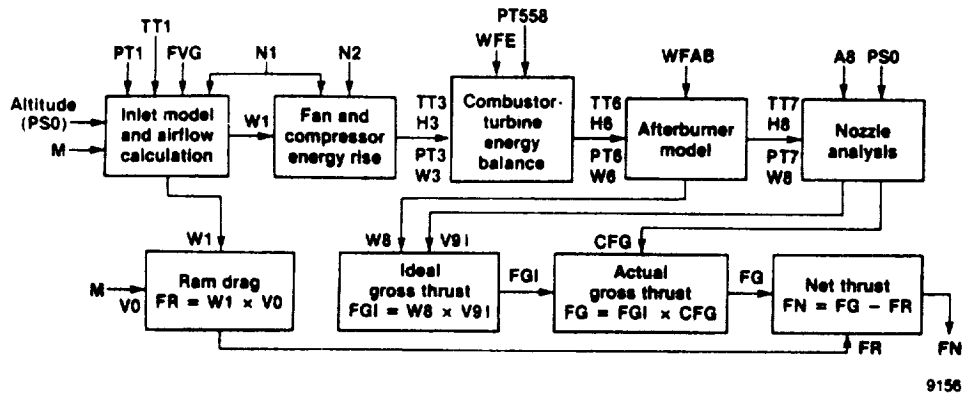


Figure 11. F404 in-flight thrust flow chart.

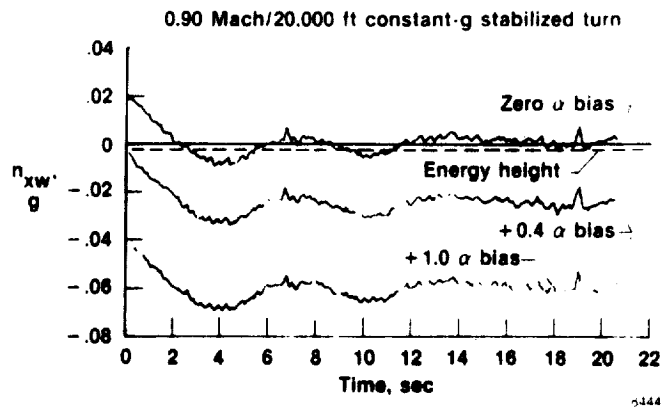


Figure 12. Energy height compared with accelerometer method.

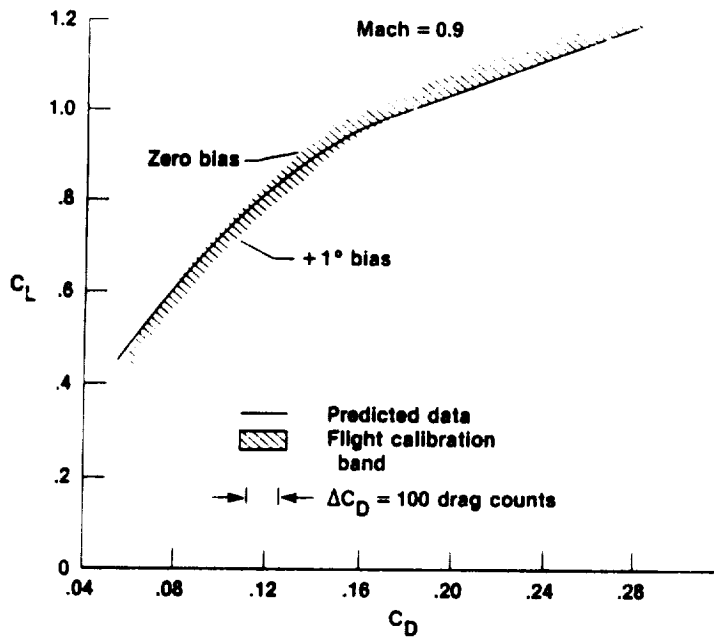


Figure 13. Angle-of-attack calibration uncertainty effects.

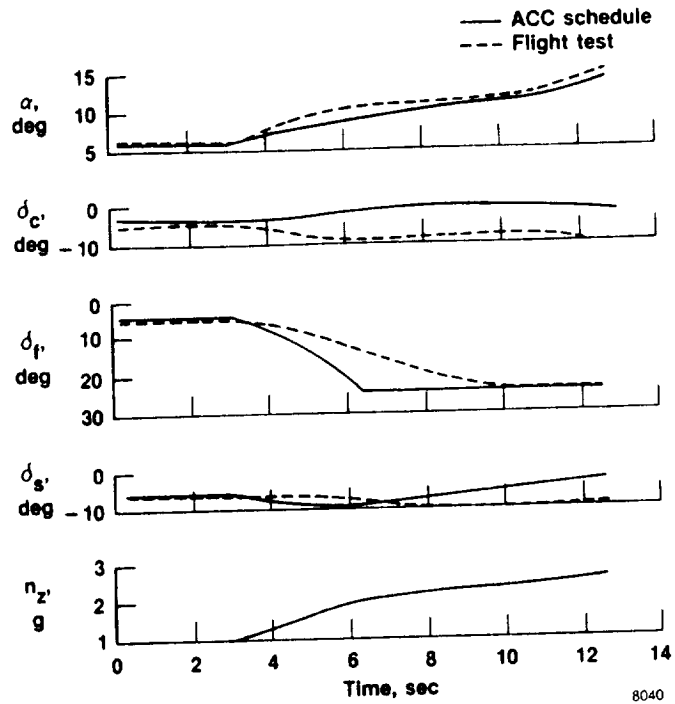


Figure 14. Off-ACC schedule effects.

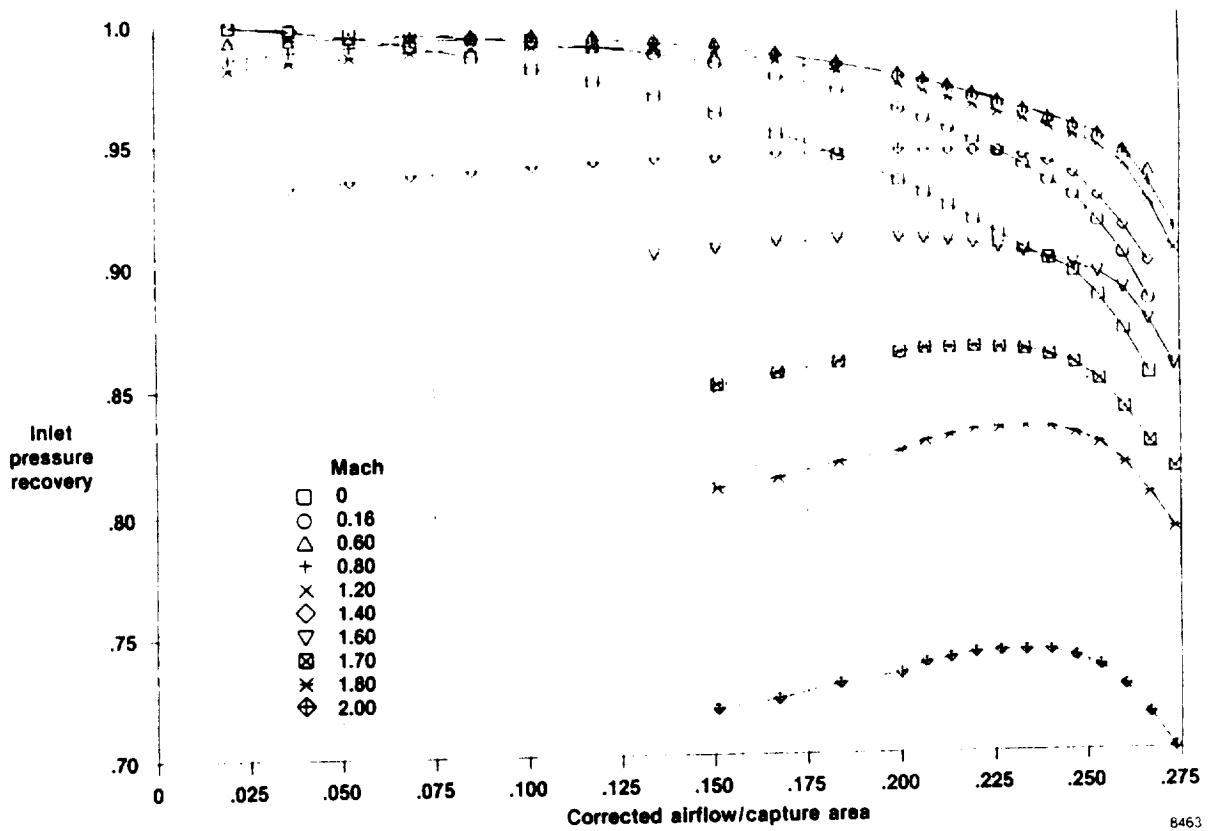


Figure 15. X-29/F404 inlet recovery factor.

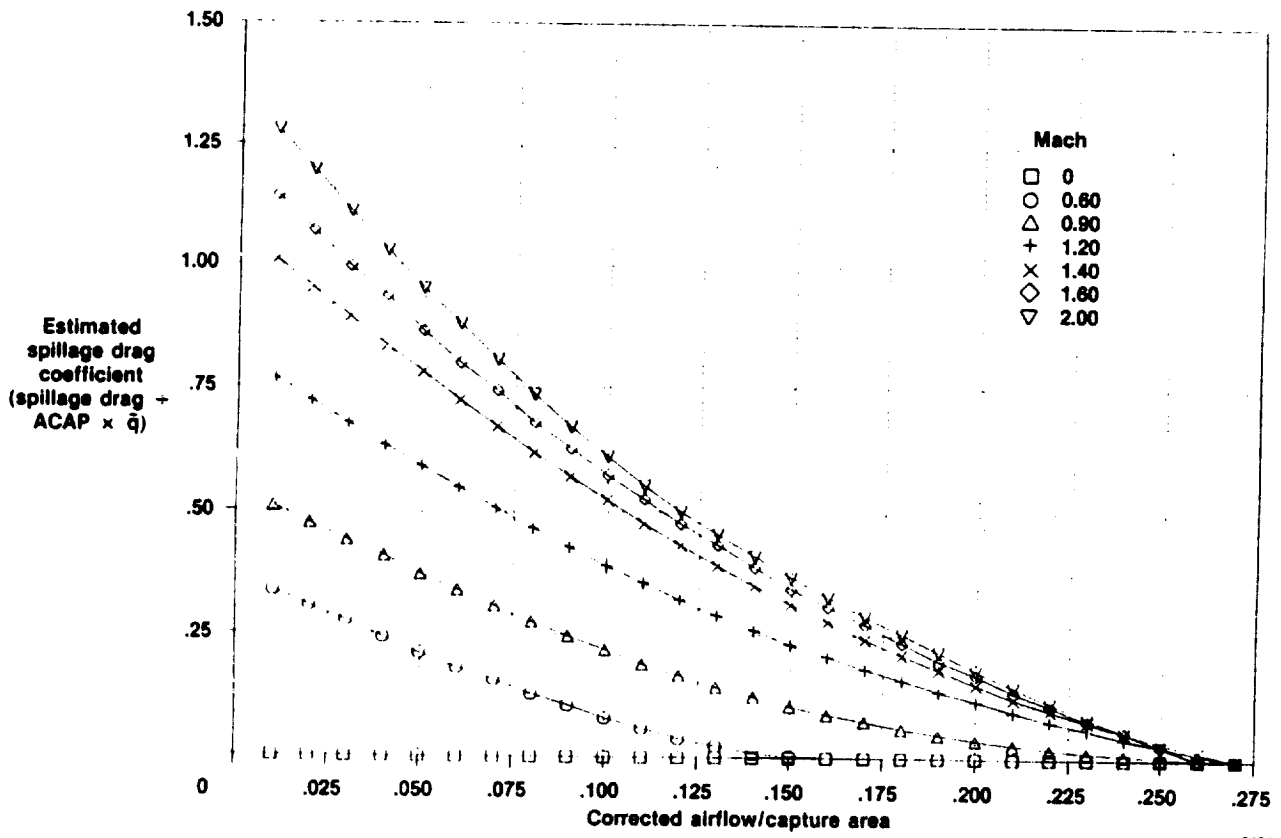


Figure 16. X-29 estimated inlet spillage drag.

8464



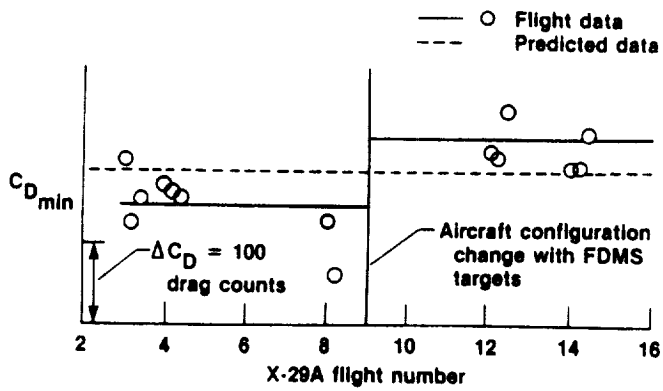


Figure 18. FDMS drag increment.

6011

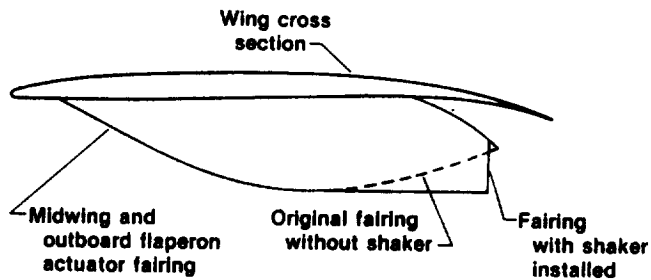


Figure 19. Flaperon shaker aerodynamic fairing modification.

6012

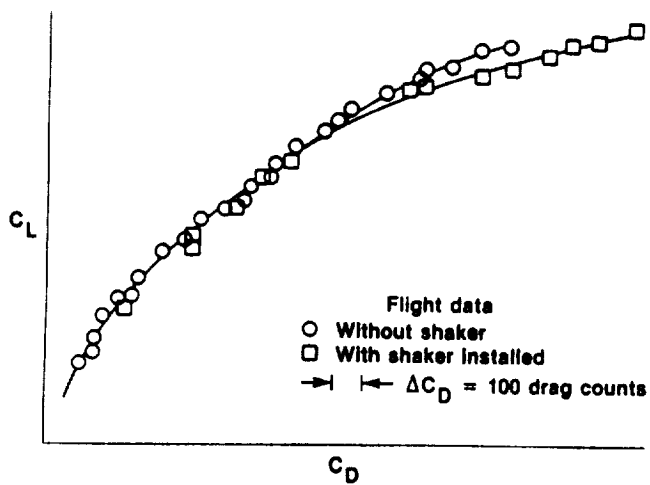


Figure 20. Flaperon shaker system drag increment.

6013

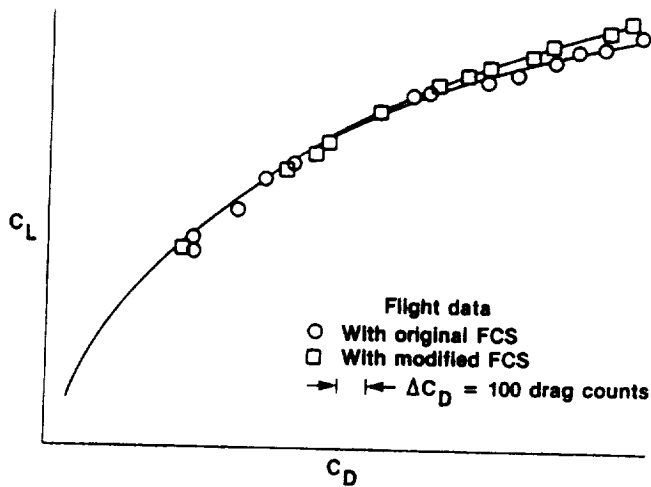
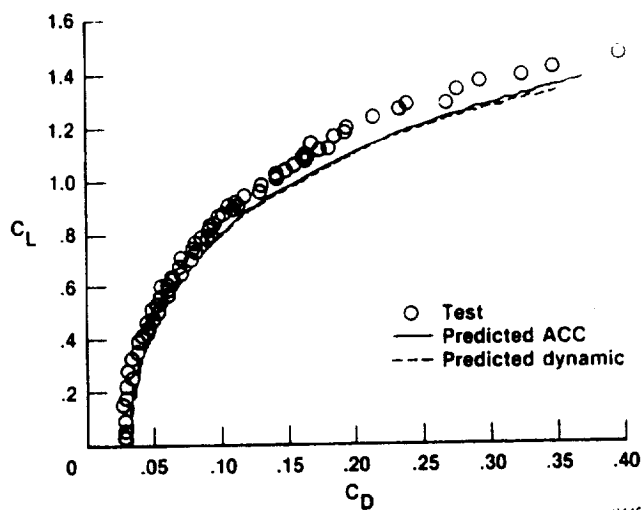
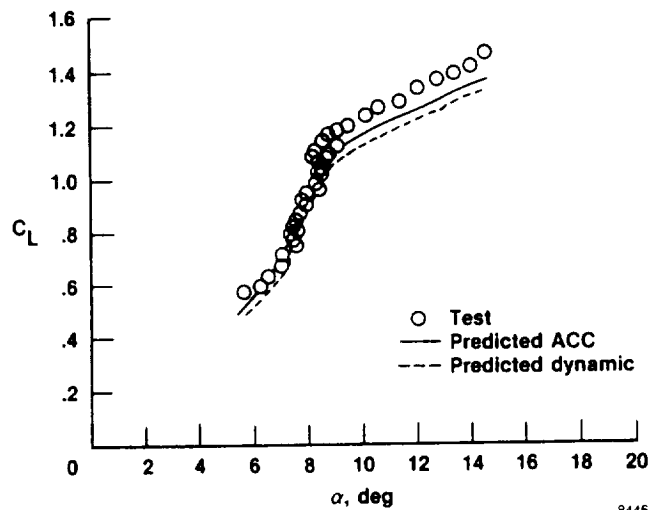


Figure 21. Flight control system modification drag effect.

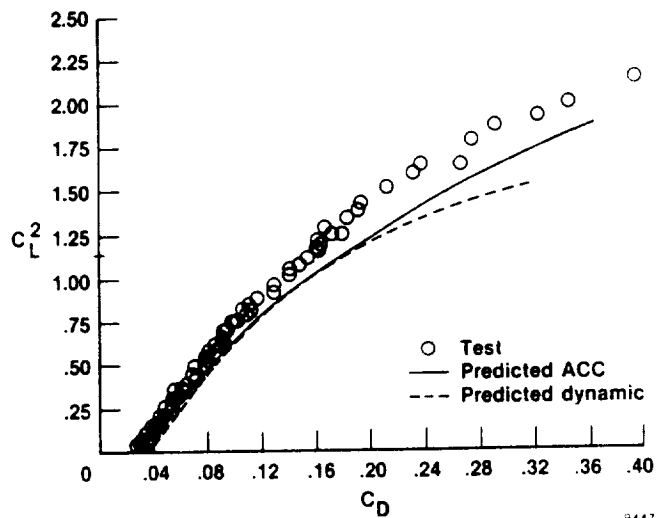
6014



(a) Drag polar,  $C_L - C_D$ .

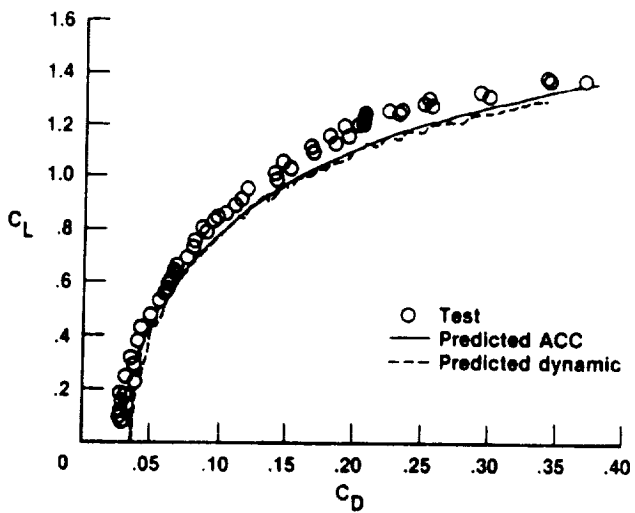


(b) Lift curve,  $C_L - \alpha$ .



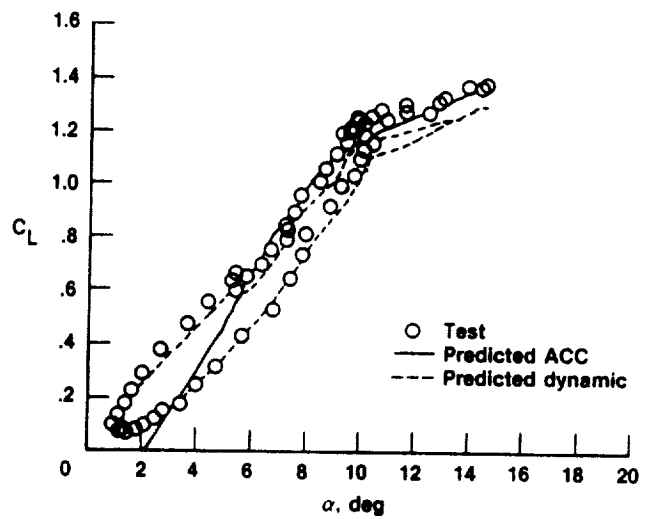
(c)  $C_L^2 - C_D$ .

Figure 22. Comparison of flight-measured and predicted aerodynamic characteristics,  $M = 0.60$ , altitude = 30,000 ft.



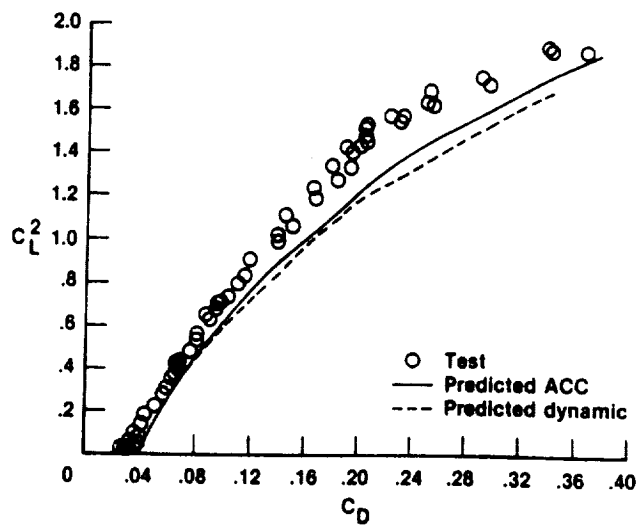
(a) Drag polar,  $C_L - C_D$ .

8448



(b) Lift curve,  $C_L - \alpha$ .

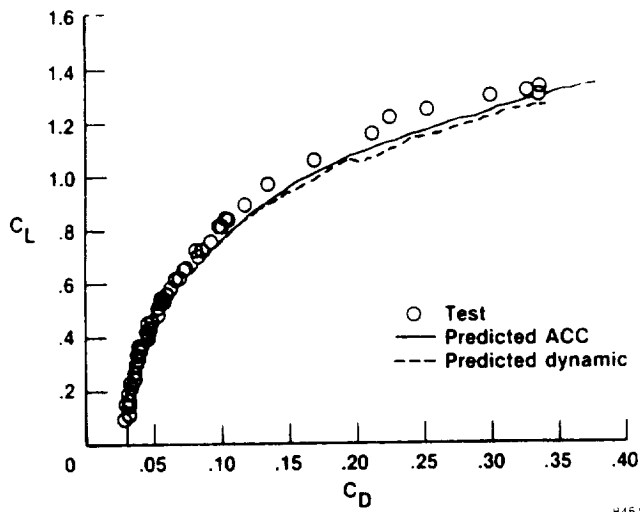
8449



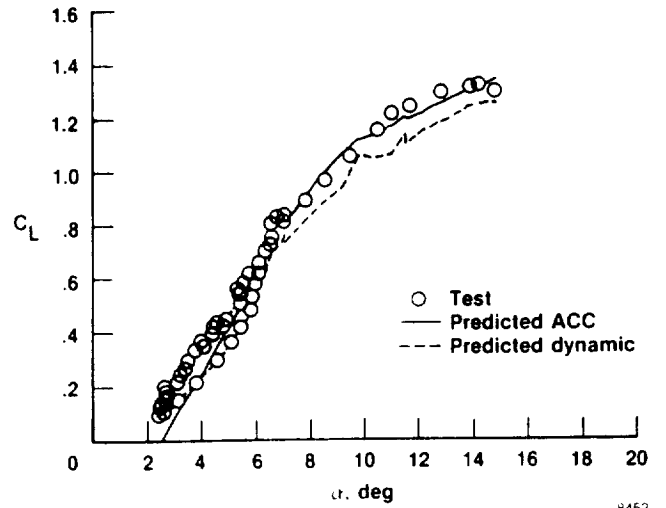
(c)  $C_L^2 - C_D$ .

8450

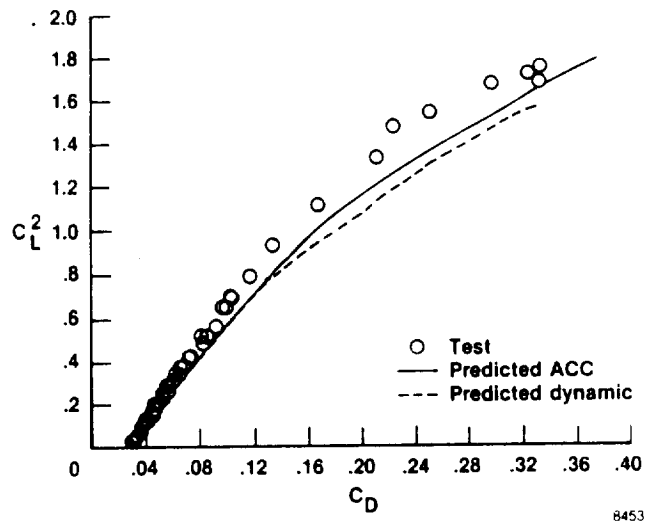
Figure 23. Comparison of flight-measured and predicted aerodynamic characteristics,  $M = 0.70$ , altitude = 40,000 ft.



(a) Drag polar,  $C_L - C_D$ .

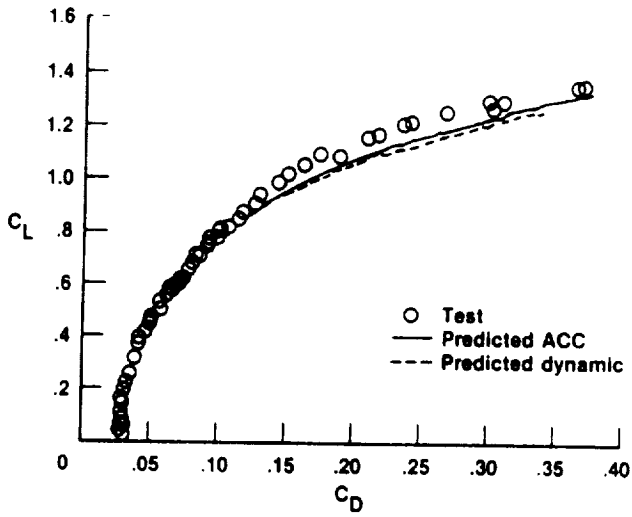


(b) Lift curve,  $C_L - \alpha$ .

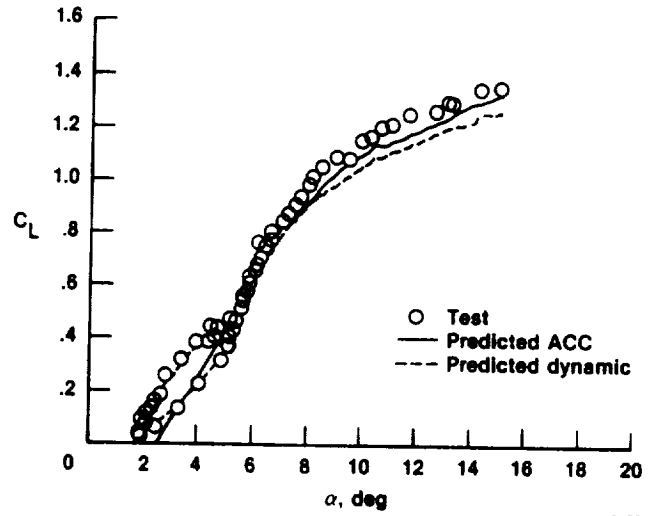


(c)  $C_L^2 - C_D$ .

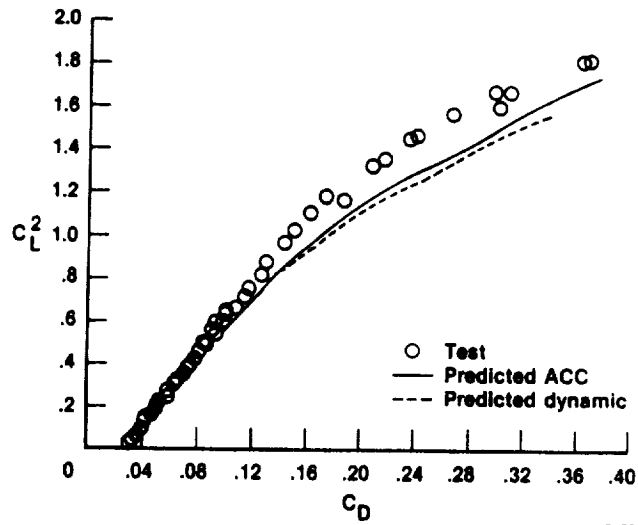
Figure 24. Comparison of flight-measured and predicted aerodynamic characteristics,  $M = 0.80$ , altitude = 40,000 ft.



(a) Drag polar,  $C_L - C_D$ .

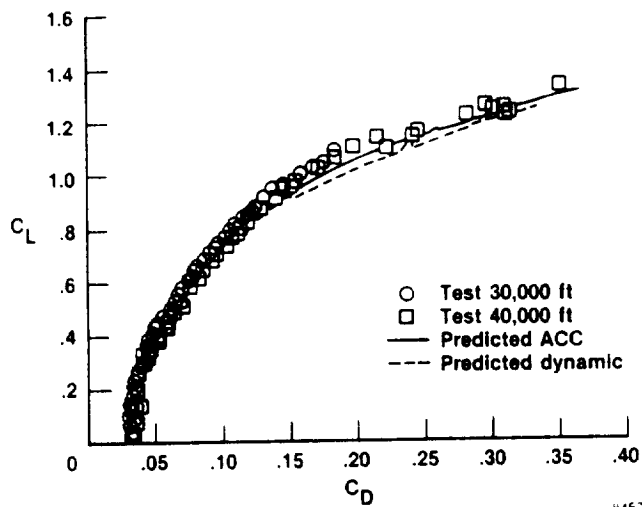


(b) Lift curve,  $C_L - \alpha$ .

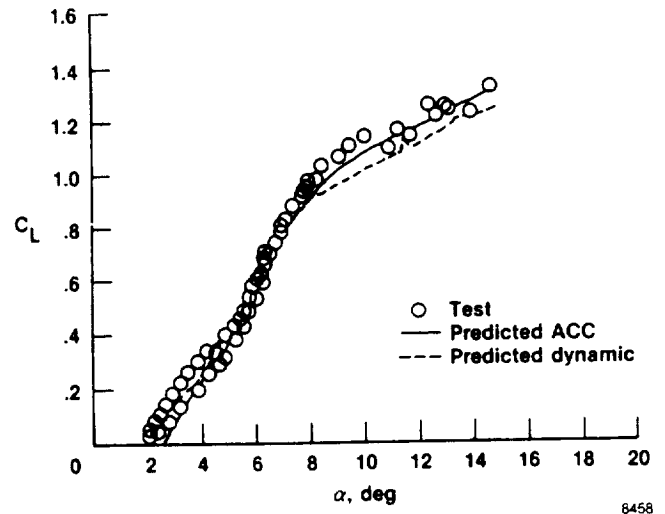


(c)  $C_L^2 - C_D$ .

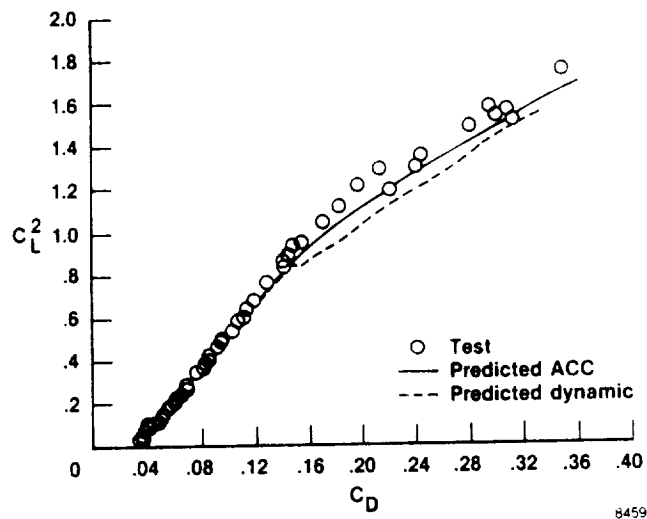
Figure 25. Comparison of flight-measured and predicted aerodynamic characteristics,  $M = 0.85$ , altitude = 40,000 ft.



(a) Drag polar,  $C_L - C_D$ .

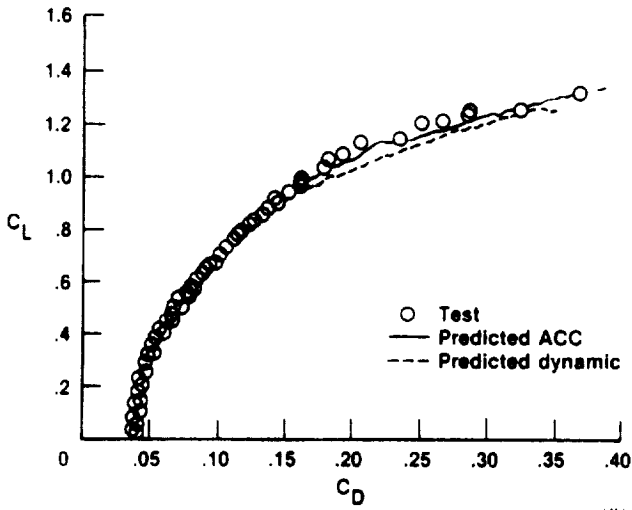


(b) Lift curve,  $C_L - \alpha$ .

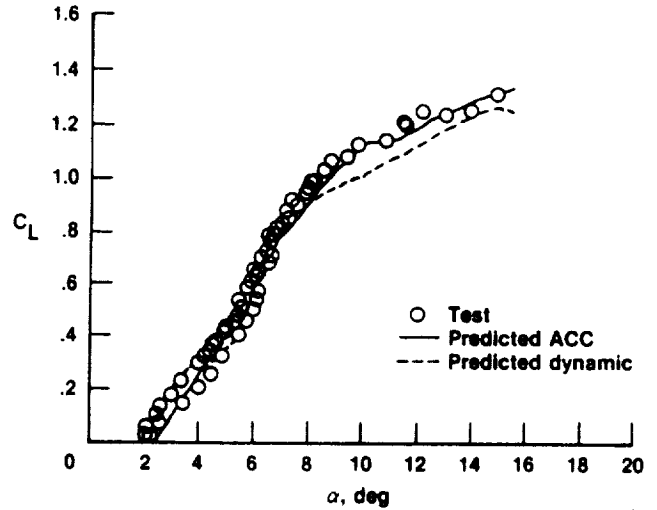


(c)  $C_L^2 - C_D$ .

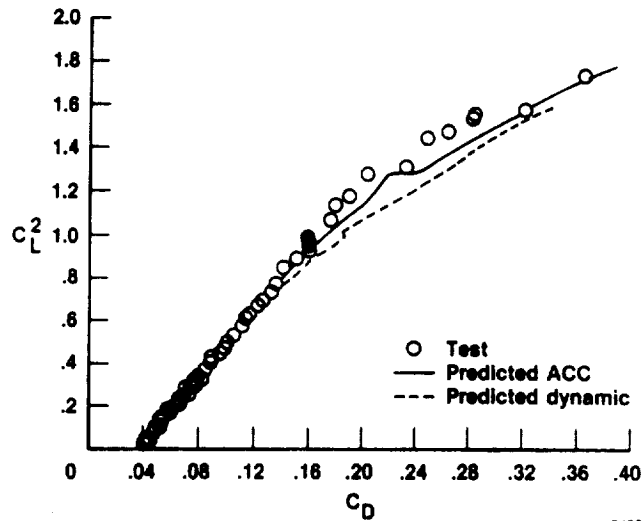
Figure 26. Comparison of flight-measured and predicted aerodynamic characteristics,  $M = 0.90$ , altitude = 30,000 and 40,000 ft.



(a) Drag polar,  $C_L - C_D$ .



(b) Lift curve,  $C_L - \alpha$ .



(c)  $C_L^2 - C_D$ .

Figure 27. Comparison of flight-measured and predicted aerodynamic characteristics,  $M = 0.95$ , altitude = 40,000 ft.

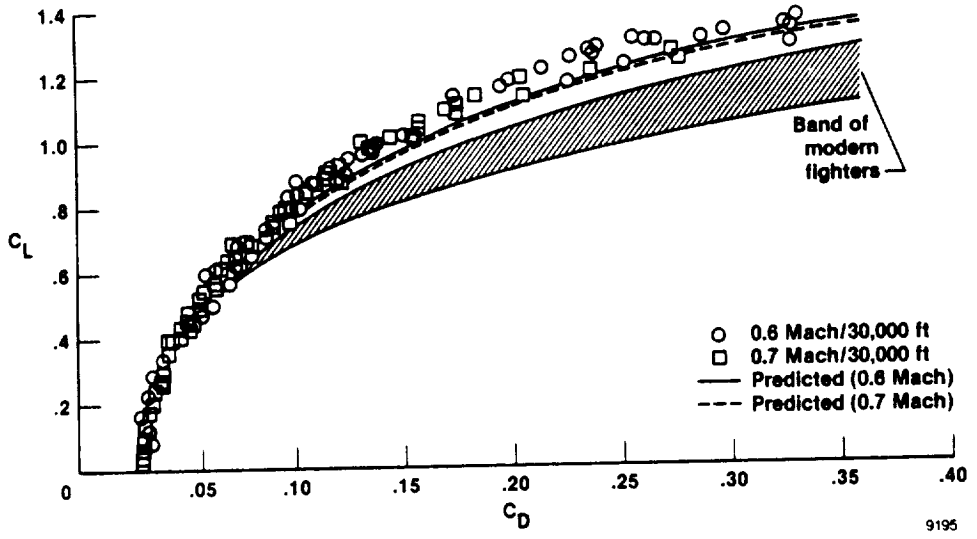


Figure 28. X-29A drag polar comparison to current fighter aircraft.



# Report Documentation Page

1. Report No. NASA TM-100409		2. Government Accession No.		3. Recipient's Catalog No.	
4. Title and Subtitle Preliminary Flight-Determined Subsonic Lift and Drag Characteristics of the X-29A Forward-Swept-Wing Airplane				5. Report Date August 1989	
				6. Performing Organization Code	
7. Author(s) John W. Hicks and Thomas Huckabone				8. Performing Organization Report No. H-1431	
				10. Work Unit No. RTOP 533-02-51	
9. Performing Organization Name and Address NASA Ames Research Center Dryden Flight Research Facility P.O. Box 273, Edwards, CA 93523-5000				11. Contract or Grant No.	
				13. Type of Report and Period Covered Technical Memorandum	
12. Sponsoring Agency Name and Address National Aeronautics and Space Administration Washington, DC 20546				14. Sponsoring Agency Code	
				15. Supplementary Notes	
16. Abstract <p>The X-29A subsonic lift and drag characteristics determined, met, or exceeded predictions, particularly with respect to the drag polar shapes. Induced drag levels were as great as 20 percent less than wind tunnel estimates, particularly at coefficients of lift above 0.8. Drag polar shape comparisons with other modern fighter aircraft showed the X-29A to have a better overall aircraft aerodynamic Oswald efficiency factor for the same aspect ratio. Two significant problems arose in the data reduction and analysis process. These included uncertainties in angle-of-attack upwash calibration and effects of maneuver dynamics on drag levels. The latter problem resulted from significantly improper control surface automatic camber control scheduling. Supersonic drag polar results were not obtained during this phase because of a lack of engine instrumentation to measure afterburner fuel flow.</p>					
17. Key Words (Suggested by Author(s)) Drag polar, flight test, forward-swept wing, subsonic, X-29A			18. Distribution Statement  Subject category 05		
19. Security Classif. (of this report) Unclassified		20. Security Classif. (of this page) Unclassified		21. No. of pages 42	22. Price A03



